The Astrophysical Journal, 978:17 (18pp), 2025 January 01 https://doi.org/10.3847/1538-4357/ad8f36

MAGAZ3NE: Evidence for Galactic Conformity in $z \gtrsim 3$ Protoclusters*

Ian McConachie[1,2], Gillian Wilson[2,3], Ben Forrest[2,4], Z. Cemile Marsan[5], Adam Muzzin[5], M. C. Cooper[6], Marianna Annunziatella[7], Danilo Marchesini[8], Percy Gomez[9], Wenjun Chang[2], Stephanie M. Urbano Stawinski[6], Michael McDonald[2], Tracy Webb[10], Allison Noble[11,12], Brian C. Lemaux[4,13], Ekta A. Shah[4], Priti Staab[4], Lori M. Lubin[4], and Roy R. Gal[14]

[1] Department of Astronomy, University of Wisconsin–Madison, 475 N. Charter St., Madison, WI 53706 USA, USA; ian.mcconachie@wisc.edu
[2] Department of Physics and Astronomy, University of California, Riverside, 900 University Avenue, Riverside, CA 92521, USA
[3] Department of Physics, University of California, Merced, 5200 North Lake Road, Merced, CA 92543, USA
[4] Department of Physics and Astronomy, University of California, Davis, One Shields Avenue, Davis, CA 95616, USA
[5] Department of Physics and Astronomy, York University, 4700, Keele Street, Toronto, ON MJ3 1P3, Canada
[6] Department of Physics and Astronomy, University of California, Irvine, 4129 Reines Hall, Irvine, CA, USA
[7] Centro de Astrobiología (CSIC-INTA), Ctra de Torrejón a Ajalvir, km 4, E-28850 Torrejón de Ardoz, Madrid, Spain
[8] Department of Physics & Astronomy, Tufts University, MA 02155, USA
[9] W.M. Keck Observatory, 65-1120 Mamalahoa Hwy., Kamuela, HI 96743, USA
[10] Department of Physics, McGill Space Institute, McGill University, 3600 rue University, Montréal, QC H3A 2T8, Canada
[11] School of Earth and Space Exploration, Arizona State University, Tempe, AZ 85287, USA
[12] Beus Center for Cosmic Foundations, Arizona State University, Tempe, AZ 85287, USA
[13] Gemini Observatory, NSF's NOIRLab, 670 N. A'ohoku Place, Hilo, HI 96720, USA
[14] Institute for Astronomy, University of Hawai'i, 2680 Woodlawn Drive, Honolulu, HI 96822, USA
Received 2023 September 21; revised 2024 October 10; accepted 2024 November 4; published 2024 December 20

Abstract

We examine the quiescent fractions of massive galaxies in six $z \gtrsim 3$ spectroscopically confirmed protoclusters in the COSMOS field, one of which is newly confirmed and presented here. We report the spectroscopic confirmation of MAGAZ3NE J100143+023021 at $z = 3.122^{+0.007}_{-0.004}$ by the Massive Ancient Galaxies At $z > 3$ NEar-infrared (MAGAZ3NE) survey. MAGAZ3NE J100143+023021 contains a total of 79 protocluster members (28 spectroscopic and 51 photometric). Three spectroscopically confirmed members are star-forming ultramassive galaxies (UMGs; $\log(M_\star/M_\odot) > 11$), the most massive of which has $\log(M_\star/M_\odot) = 11.15^{+0.05}_{-0.06}$. Combining Keck/MOSFIRE spectroscopy and the COSMOS2020 photometric catalog, we use a weighted Gaussian kernel density estimator to map the protocluster and measure its total mass $2.25^{+1.55}_{-0.65} \times 10^{14}\,M_\odot$ in the dense "core" region. For each of the six COSMOS protoclusters, we compare the quiescent fraction to the status of the central UMG as star-forming or quiescent. We observe that galaxies in these protoclusters appear to obey galactic conformity: Elevated quiescent fractions are found in protoclusters with *UVJ*-quiescent UMGs and low quiescent fractions are found in protoclusters containing *UVJ* star-frming UMGs. This correlation of star formation/quiescence in UMGs and the massive galaxies nearby in these protoclusters is the first evidence for the existence of galactic conformity at $z > 3$. Despite disagreements over mechanisms behind conformity at low redshifts, its presence at these early cosmic times would provide strong constraints on the physics proposed to drive galactic conformity.

Unified Astronomy Thesaurus concepts: Galaxy evolution (594); Galaxy environments (2029); High-redshift galaxies (734); High-redshift galaxy clusters (2007)

1. Introduction

It is well established that in the local Universe, the properties of galaxies exhibit a bimodal distribution. Classifying galaxies based on color, star formation rate (SFR), and morphology creates two distinct populations: red, quiescent "early-type" and blue, star-forming "late-type" galaxies (e.g., I. Strateva et al. 2001; G. Kauffmann et al. 2003; I. K. Baldry et al. 2004; J. Moustakas et al. 2013). Additionally, these properties have been shown to depend on the local environment, with passive early-type galaxies frequently residing in high-density regions (i.e., clusters) whereas star-forming late-type galaxies more commonly exist in lower-density regions, i.e., the "field" (A. J. Oemler 1974; A. Dressler 1980; P. L. Gómez et al. 2003; T. Goto et al. 2003; G. Kauffmann et al. 2004; Y.-j. Peng et al. 2010). Within groups and clusters, galaxies are strongly affected by environmental processes such as ram pressure stripping (J. E. Gunn & J. R. I. Gott 1972), "strangulation" (R. B. Larson et al. 1980), and "galaxy harassment" (B. Moore et al. 1996), which are thought to give rise to this disparity between galaxy populations.

While the distinction between star-forming and quiescent galaxies is present at earlier cosmic times, the clear bimodality appears to erode with redshift (K. E. Whitaker et al. 2011; A. Muzzin et al. 2013; C. M. S. Straatman et al. 2016; J. R. Weaver et al. 2022). The redshift evolution of this relationship between the density of a galaxy's environment and the galaxy's SFR is a subject of debate in galaxy evolution.

* Some of the data presented herein were obtained at the W. M. Keck Observatory, which is operated as a scientific partnership among the California Institute of Technology, the University of California, and the National Aeronautics and Space Administration. The Observatory was made possible by the generous financial support of the W. M. Keck Foundation.

Quenching has been linked to the density of the environment at $z \sim 1$ (M. C. Cooper et al. 2007, 2010; A. Muzzin et al. 2012). Studies of galaxy clusters at these intermediate redshifts indicate that the same mechanisms are at work at this epoch (e.g., M. L. Balogh et al. 2016, 2017; J. B. Nantais et al. 2016; R. Foltz et al. 2018; L. Shen et al. 2019; R. F. J. van der Burg et al. 2020; K. Webb et al. 2020; D. C. Baxter et al. 2022; Z. Mao et al. 2022; D. C. Baxter et al. 2023; S. Mei et al. 2023), though the clear anticorrelation between galaxy overdensity and SFR seen in the local Universe may break down (D. Elbaz et al. 2007; M. C. Cooper et al. 2008) by $z \sim 1$ (however, it may still hold in clusters; see A. R. Tomczak et al. 2017; B. C. Lemaux et al. 2017; B. C. Lemaux et al. 2019; A. R. Tomczak et al. 2019). Observations of protoclusters often reveal strongly star-forming populations (e.g., S. C. Chapman et al. 2009; H. Dannerbauer et al. 2014; C. M. Casey et al. 2015; C.-L. Hung et al. 2016; B. Forrest et al. 2017), leading B. C. Lemaux et al. (2022) to conclude that at $z > 2$, star formation instead *increases* with galaxy overdensity (though see also S. I. Muldrew et al. 2018; N. Chartab et al. 2020). In recent years, however, the assumed ubiquity of star-forming galaxies in protoclusters (C. M. Casey 2016) has been challenged by the discovery of massive, quiescent galaxies in protocluster systems (B. S. Kalita et al. 2021; M. Kubo et al. 2021; K. Shi et al. 2021; I. McConachie et al. 2022; K. Ito et al. 2023).

In addition to the clear dependence of a galaxy's properties on the density of its environment at low redshifts, it has been demonstrated that the properties of nearby galaxies are also correlated, in both clusters and the field. At $z \sim 0$, S. M. Weinmann et al. (2006) showed that the satellite galaxies around massive early-type centrals tended to also be early types, while late-type centrals tended to have late-type satellites. Subsequent studies of this phenomenon, dubbed "galactic conformity," have demonstrated in the low-redshift Universe that the star formation or quiescence of satellites is strongly linked to the star formation or quiescence of the central—based on observations (A. J. Ross & R. J. Brunner 2009; G. Kauffmann et al. 2010, 2013; W. Wang & S. D. M. White 2012; J. I. Phillips et al. 2014, 2015; G. Kauffmann 2015, 2018; C. Knobel et al. 2015; A. Paranjape et al. 2015; A. M. Berti et al. 2017; V. F. Calderon et al. 2018; S. Sun et al. 2018; M. Treyer et al. 2018; J. A. Otter et al. 2020; K. Wang et al. 2023), simulations (A. P. Hearin et al. 2015; A. D. Bray et al. 2016; A. P. Hearin et al. 2016; M. Kerscher 2018), and semianalytical models (SAMS; B. M. B. Henriques et al. 2017; L. P. T. Sin et al. 2017; I. Lacerna et al. 2018; Z.-Y. Man et al. 2019; L. P. T. Sin et al. 2019). While S. M. Weinmann et al. (2006) used a combination of color and specific star formation rate (sSFR) to classify galaxies as early type or late type, galactic conformity specific to color (e.g., Y. Zu & R. Mandelbaum 2018), sSFR (e.g., V. F. Calderon et al. 2018), and morphology (J. A. Otter et al. 2020) have all been observed (at low redshift) with data sets from large spectroscopic surveys.

Evidence for galactic conformity has been found as high as $z \sim 2$ in both observations and theoretical models. In a comparison between low-redshift observations and models, M. Ayromlou et al. (2022) found that not only did the IllustrisTNG 300 Mpc (D. Nelson et al. 2019) simulation and a recent L-GALAXIES SAM (M. Ayromlou et al. 2021) generally agree with observed (low-redshift) conformity, but these models also showed signal for galactic conformity out to at least $z \sim 2$. At higher redshifts, observational studies often rely on photometric catalogs in deep fields and classify galaxies as star-forming or quiescent by their rest-frame $U - V$ and $V - J$ colors. An analysis of galactic conformity in the UKIRT Infrared Deep Sky Survey (UKIDSS; A. Lawrence et al. 2007) Ultra Deep Survey (UDS; O. Almaini et al. 2024, in preparation) at $0.4 < z < 1.9$ found elevated quenched satellite fractions around quiescent centrals within a few hundred kpc to a 3σ significance (W. G. Hartley et al. 2015). Meanwhile, with photometric data from the UDS, UltraVISTA (H. J. McCracken et al. 2012; A. Muzzin et al. 2013), and ZFOURGE (C. M. S. Straatman et al. 2015) catalogs, L. Kawinwanichakij et al. (2016) examined galactic conformity in four different redshift bins from $0.3 < z < 2.5$ (only the ZFOURGE data set was used in the highest redshift bin as it was the only one deep enough to detect satellites) and also detected conformity. The presence of galactic conformity at such high redshifts suggests that satellite quenching may not be due solely to environmental effects but instead may also be influenced by internal processes. The authors speculate that either there must be another source of conformity (e.g., feedback from star formation or active galactic nuclei drives quenching, as was suggested in W. G. Hartley et al. 2015) or galactic conformity must extend to higher redshifts.

We present here the first evidence for galactic conformity at $z \gtrsim 3$ in overdense environments around ultramassive galaxies ($\log(M_\star/M_\odot) > 11$; UMGs). The paper is organized as follows: We select and describe the photometric catalog and six spectroscopically confirmed COSMOS protocluster systems at $2.75 < z < 4$ used in this work in Section 2. In Section 3, we present the target selection, spectroscopic observations, data reduction, and determination of spectroscopic redshifts of the newly identified protocluster system, MAGAZ3NE J100143 +023021. In Section 4, we determine photometric members of each COSMOS protocluster. In Section 5, we calculate rest-frame $U - V$ and $V - J$ colors and quiescent fractions for each protocluster. We discuss the newly confirmed protocluster MAGAZ3NE J100143+023021 and the observed galactic conformity in Section 6, and we summarize our main conclusions in Section 7. We assume $\Omega_m = 0.3$, $\Omega_\lambda = 0.7$, and $H_0 = 70\,\mathrm{km\,s^{-1}\,Mpc^{-1}}$ throughout. All magnitudes are on the AB system (J. B. Oke & J. E. Gunn 1983).

2. The COSMOS Field

The COSMOS-UltraVISTA field contains the deepest, highest-quality multi-passband optical, infrared, and Spitzer IRAC imaging available over degree scales. Multi-passband imaging taken as part of the COSMOS survey (P. Capak et al. 2007), CFHT-Deep Legacy Survey (H. Hildebrandt et al. 2009), the Subaru Strategic Program (H. Aihara et al. 2018), and UltraVISTA (H. J. McCracken et al. 2012) provides an unparalleled set of photometric measurements in multiple bands, which can be used to estimate photometric redshifts, stellar masses, and rest-frame *UVJ* colors through spectral energy distribution (SED) modeling. The field is also covered by the Galaxy Evolution Explorer, Chandra, XMM-Newton, Herschel, SCUBA, and the Very Large Array, as well as spectroscopic surveys such as zCOSMOS (S. J. Lilly et al. 2007), LEGA-C (A. van der Wel et al. 2016), DEIMOS-10k (G. Hasinger et al. 2018), and VUDS (O. Le Fèvre et al. 2015).

The unique quality and diversity of observations in the COSMOS-UltraVISTA field has facilitated the discovery of

protoclusters using a variety of techniques. These include X-ray emission (A. Finoguenov et al. 2007; T. Wang et al. 2016), overdensities in photometric redshift (e.g., Y.-K. Chiang et al. 2014; N. B. Sillassen et al. 2022; M. Brinch et al. 2023), distant red galaxies, LAEs, HAEs (J. E. Geach et al. 2012; Y. Koyama et al. 2021), radio sources (E. Daddi et al. 2017), or 3D Lyα forest tomography (K.-G. Lee et al. 2014; A. B. Newman et al. 2020). Notable spectroscopically confirmed protoclusters at $z > 2$ that have been discovered in the COSMOS-UltraVISTA field include systems at $z = 2.095$ (L. R. Spitler et al. 2012; T. Yuan et al. 2014; C. M. Casey 2016; C.-L. Hung et al. 2016; K.-V. H. Tran et al. 2017; J. A. Zavala et al. 2019), $z = 2.16$ (Y. Koyama et al. 2021), $z = 2.232$ ("CC2.2"; B. Darvish et al. 2020), $z = 2.30$ ("COSTCO-I"; K.-G. Lee et al. 2016; M. Ata et al. 2022), $z = 2.446$ ("Hyperion"; C. Diener et al. 2013; Y.-K. Chiang et al. 2014; C. M. Casey et al. 2015; Y.-K. Chiang et al. 2015; C. Diener et al. 2015; C. M. Casey 2016; K.-G. Lee et al. 2016; O. Cucciati et al. 2018; J. A. Zavala et al. 2019; A. B. Newman et al. 2020; J. B. Champagne et al. 2021), $z = 2.506$ ("CLJ1001"; T. Wang et al. 2016; E. Daddi et al. 2017), $z = 2.77$ ("QO-1000"; K. Ito et al. 2023), $z = 2.895$ (O. Cucciati et al. 2014), $z = 2.91$ ("RO-1001"; E. Daddi et al. 2021; B. S. Kalita et al. 2021), $z \sim 3.3$ ("Elentári"; B. Forrest et al. 2023, 2024), $z \sim 3.37$ ("MAGAZ3NE J095924+022537" and "MAGAZ3NE J100028+023349"; I. McConachie et al. 2022, hereafter McC22), $z \sim 4.57$ ("PCl J1001+0220"; B. C. Lemaux et al. 2018), $z \sim 5.3$ (P. L. Capak et al. 2011), and $z = 5.667$ (R. Pavesi et al. 2018).

2.1. COSMOS2020 Photometric Catalog

To characterize galaxies in $z \gtrsim 3$ protoclusters and the coeval field, we utilize the COSMOS2020 catalogs (hereafter C2020; J. R. Weaver et al. 2022). These catalogs contain imaging data from the UltraVISTA Data Release Four (H. J. McCracken et al. 2012), which effectively homogenizes K_s depth between the deep and ultradeep regions, giving near-uniform coverage of the field (within 0.4 mag in K_s; H. J. McCracken et al. 2012). The C2020 catalogs come in two forms: the CLASSIC catalog and the FARMER catalog. The fluxes in the CLASSIC catalog are extracted via "classic" aperture photometry. 2″ and 3″ diameter apertures are extracted using `SExtractor` in "dual-image mode" on PSF-homogenized images (E. Bertin & S. Arnouts 1996) and an $izYJHK_s$ detection image. The Farmer catalog utilizes `The Tractor` (driven by `The Farmer`, J. R. Weaver et al. 2023) to detect sources and extract photometry. For our photometric analysis here, we utilize the CLASSIC catalog as it covers a greater footprint with fewer, smaller regions masked out.

The C2020 catalogs also contain best-fit photometric redshifts, rest-frame colors, and quantities such as SFR, stellar mass, and ages, calculated using both `EazyPy` (G. B. Brammer et al. 2008) and `LePhare` (O. Ilbert et al. 2006), which produce broadly similar values. In this work, we use `EazyPy` to calculate RF colors and galaxy properties for galaxies with spectroscopic redshifts; otherwise, we adopt the `EazyPy` values presented in the catalog. When refitting galaxies at their $z_{\rm spec}$, we follow the same method as J. R. Weaver et al. (2022), briefly summarized below.

For each source, the magnitude offsets from J. R. Weaver et al. (2022) were applied to MegaCam/CFHU u and u^*, HSC/Subaru $grizy$, VIRCAM/VISTA $YJHK_s$ broad bands, 12 Suprime-Cam/Subaru medium bands ($IB427$, $IB464$, $IA484$, $IB505$, $IA527$, $IB574$, $IA624$, $IA679$, $IB709$, $IA738$, $IA767$, and $IB827$), and IRAC channels 1 and 2. The photometry was then fit to a set of 13 templates derived using the flexible Stellar Population Synthesis models (C. Conroy et al. 2009; C. Conroy & J. E. Gunn 2010). The templates were produced using a range of dust attenuation and log-normal star formation histories, and therefore have associated physical parameters (e.g., stellar mass, SFR). This means that when constructing a best-fit model with nonnegative linear combination of templates, these physical parameters will also "propagate through" to the final model. 1σ uncertainties on these physical parameters are taken from the 16th and 84th percentiles of 100 fits drawn from the best-fit template error function (we note that these uncertainties are likely underestimated, however, as `EazyPy` does not marginalize over the redshift error).

Table 1
$z \gtrsim 3$ COSMOS Protoclusters

Name	UMG ID[a]	$z_{\rm spec}$	References
QO-1000	301560	2.77	K. Ito et al. (2023)
VPC-1000	570315[b]	2.90	O. Cucciati et al. (2014)
RO-1001	965181	2.91	E. Daddi et al. (2021)
MAG-1001	1137168	3.12	This work
MAG-0959	1064615	3.37	McC22
MAG-1000	1208085	3.38	McC22

Notes.
[a] C2020 ID of the "central" UMG as defined in Section 4.2.
[b] Photometrically selected (see Section 4.2).

2.1.1. z $\gtrsim$ 3 Protocluster Sample

In this work, we measure the quiescent fractions for six spectroscopically confirmed $z \gtrsim 3$ protoclusters. We briefly summarize the COSMOS protoclusters here and list them in Table 1, ordered by ascending redshift:

1. *QO-1000*. This protocluster was initially identified as an overdensity of quiescent galaxy candidates then targeted for spectroscopic follow-up in K. Ito et al. (2023). The four confirmed $\log(M_\star/M_\odot) > 11$ quiescent galaxies at $z = 2.77$ all show prominent absorption features. The authors also measured a quiescent fraction of $34\% \pm 11\%$ (roughly three times higher than the field value $12.9\% \pm 0.9\%$) and speculated that QO-1000 was more mature than other protoclusters and in a transition phase to a quenched galaxy cluster.
2. *VPC-1000*. A spectroscopic overdensity of 12 emission-line galaxies at $z = 2.90$ was identified in the VUDS survey in O. Cucciati et al. (2014). A name for this protocluster was not provided, so we apply the prefix VPC (short for VUDS Protocluster) to its R.A./decl. coordinates. Spectroscopic redshifts and target coordinates were not published for this structure.
3. *RO-1001*. This protogroup first identified as an overdensity of radio sources in COSMOS with three tightly grouped massive galaxies at $z_{\rm spec} = 2.91$ from ALMA spectroscopy in E. Daddi et al. (2021). We also examined the radio overdensities/LABs RO-0959 at $z = 3.10$ and RO-0958 at $z = 3.30$ from E. Daddi et al. (2022) and did not find that they coincided with significant massive galaxy overdensities (see Section 4).

4. *MAGAZ3NE J100143+023021*. An overdensity of spectroscopic redshifts at $z = 3.12$ confirmed by the Massive Ancient Galaxies at $Z > 3$ NEar-infrared (MAGAZ3NE) survey, as described in Section 3. This structure is also independently identified in the One-hundred-deg^2 DECam Imaging in Narrowbands (ODIN) survey (V. Ramakrishnan et al. 2023; K.-S. Lee et al. 2024).
5. *MAGAZ3NE J095924+022537*. This galaxy protocluster (hereafter MAG-0959) at $z = 3.37$ was first presented in McC22. It contains a *UVJ*-quiescent UMG ("COS-DR3-179370" in B. Forrest et al. 2020b and "C1-15182" in Z. C. Marsan et al. 2017) and remarkably also features an elevated fraction of quiescent galaxies (which appeared to be mass dependent; $QF = 73.3\%^{+26.7}_{-16.9}$ at $\log(M_\star/M_\odot) \geqslant 11$) relative to the coeval field. Later observations and analyses reveal that this protocluster is the most overdense substructure, "S1," within the extended protosupercluster Elentári at $z \sim 3.3$ (B. Forrest et al. 2023, 2024).
6. *MAGAZ3NE J100028+023349*. Also presented in McC22, this overdensity (hereafter MAG-1000) lies at $z = 3.38$ and is separated from MAG-0959 by a projected distance 35 comoving Mpc. MAG-1000 also contains a *UVJ* star-forming UMG (first identified in Z. C. Marsan et al. 2015 and since further studied as "COS-DR3-160748" in B. Forrest et al. 2020b and "C1-23152" in Z. C. Marsan et al. 2017 and P. Saracco et al. 2020). MAG-1000 is also a substructure within Elentári ("S4"), though its physical size and halo mass is estimated to be among the smallest of the protosupercluster's individual peaks (B. Forrest et al. 2023).

3. Spectroscopic Confirmation of Protocluster MAGAZ3NE J100143+023021

The MAGAZ3NE survey seeks to confirm the existence and quantify properties of high-redshift ultramassive galaxies (UMGs, $\log(M_\star/M_\odot) > 11$) at $z > 3$ using near-infrared spectroscopy to probe the rest-frame optical wavelengths at these redshifts (B. Forrest et al. 2020a, 2020b). In B. Forrest et al. (2020b) a sample of unobscured candidate UMGs (with $\log(M_\star/M_\odot) > 11.2$, $z_{\rm phot} > 3$, $m_{K_s} < 22$)[15] was selected from the multi-passband optical-infrared catalogs of the COSMOS-UltraVISTA (Z. C. Marsan et al. 2022; A. Muzzin et al. 2024, in preparation) and VIDEO fields (M. Annunziatella et al. 2024, in preparation). The candidate UMGs were then targeted with the MOSFIRE spectrograph (I. S. McLean et al. 2010, 2012) on the W. M. Keck Observatory for spectroscopic follow-up (PI: Wilson). MOSFIRE spectra and stellar population properties (stellar mass, SFR, star formation history, quiescence) of the 16 MAGAZ3NE UMGs that have been spectroscopically confirmed to date were presented in B. Forrest et al. (2020b). A detailed study of quiescent MAGAZ3NE UMGs found that these galaxies' compact sizes and high velocity dispersions combined to give dynamical masses consistent with the derived stellar masses assuming a Chabrier initial mass function (B. Forrest et al. 2022).

A key goal of the MAGAZ3NE survey is to utilize MOSFIRE's powerful multiplexing capabilities in combination with the deep and extensive UltraVISTA Data Release 3 catalog (hereafter "DR3"; Z. C. Marsan et al. 2022; A. Muzzin et al. 2024, in preparation) to characterize not only each UMG but also its environment. MOSFIRE slits were placed on candidate UMGs and ancillary targets at similar photometric redshifts selected from the photometric catalogs to probe the environment of each UMG. In this work, we include the three strongest spectroscopic overdensities around MAGAZ3NE UMGs in our analysis. Two of these overdensities, MAG-0959 and MAG-1000, were discovered and discussed in McC22 and were shown to be substructures in the $z \sim 3.3$ protosupercluster Elentári (S1 and S4, respectively; B. Forrest et al. 2023). We present the third overdensity, MAGAZ3NE J100143+023021, in this paper.

[15] The magnitude limit was applied after the first targeted UMG, COS-DR3-179370 ($m_{K_s} = 22.14$; B. Forrest et al. 2020b; McC22), was only confirmed by detection of its strong emission lines.

Table 2
Overview of Observations

Mask	Observation Date	Exposure Time (s)	Seeing (FWHM)
K1	2020 Feb 2	4320	0.″80
K2	2021 Feb 8	9000	0.″70
K3	2021 Feb 8	8640	0.″81
NEb_1	2023 Feb 3	5400	0.″86

3.1. MOSFIRE Spectroscopic Observations and Data Reduction

Target C2020-1147901 is one of the candidate $3 < z < 4$ UMGs selected from the DR3 catalog (DR3 ID 131925) and targeted for spectroscopic follow-up as part of the MAGAZ3NE survey as described in B. Forrest et al. (2020b). As summarized in Table 2, a total of three masks centered on C2020-1147901 were observed in the *K* band (K1 through K3). Exposure times ranged between 4.3 ks and 9 ks. Filler slits on each mask were placed on DR3 targets with photometric redshift $z_{\rm phot} \pm 0.3$ of the UMG candidate's photometric redshift, with priority given to galaxies with total K_s-band magnitude brighter than $K_{s,\rm tot} = 23.0$.

A deblending error in the detection and extraction of this UMG candidate in the DR3 catalog resulted in a nearby bright object contaminating the galaxy's *Ks*-band flux. This contamination in the K_s band resulted in an incorrectly elevated stellar mass measurement. Comparisons between this source's entry in the DR3 (ID 131925), C2020 (ID 1147901), and COSMOS-UltraVISTA Data Release 1 (DR1, ID 184166; A. Muzzin et al. 2013) catalogs indicate its mass is $\log(M_\star/M_\odot) \sim 10.3$ (see ID 1147901 in Table 3). All other MAGAZ3NE UMGs and ancillary targets (B. Forrest et al. 2020b, 2022; McC22) with matches between the DR3, UltraVISTA DR1, and C2020 catalogs have consistent photometry. We also find that the best-fit stellar masses of three other ancillary targets are in excess of $\log(M_\star/M_\odot) = 11$ (C2020-1137168, C2020-1183658, and C2020-1182835; see Table 3 and Figure 1) and comprise the UMG sample in this work. For all three of these sources $m_{K_s} > 22.5$, so they were not included in the sample of candidate UMGs (as described in Section 3 and B. Forrest et al. 2020b).

One additional MOSFIRE mask (NEb_1) was observed by the Charting Cluster Construction with VUDS and ORELSE (C3VO, B. C. Lemaux et al. 2022) survey targeting the Elentàri structure at $z \sim 3.3$ (B. Forrest et al. 2023, 2024), which overlapped with the structure presented here (see dotted outline

Table 3
Properties of Spectroscopic Members of MAG-1001, Ordered by Stellar Mass

C2020 ID	Mask	α (degrees)	δ (degrees)	K_s	$z_{\rm spec}$[a]	C[b]	Stellar Mass $\log(M_\star/M_\odot)$	Age log(yr)	SFR $\log(M_\odot\ {\rm yr}^{-1})$
1137168	K1, K2, K3	150.441650	2.496970	22.60	3.1117	1	$11.15^{+0.05}_{-0.06}$	8.89	$0.69^{+0.22}_{-0.11}$
1183658	K1, K2	150.496428	2.541602	22.58	3.1372	1	$11.10^{+0.04}_{-0.04}$	8.85	$0.88^{+0.06}_{-0.06}$
1182835	K2	150.495499	2.541086	23.18	3.1274	1	$11.05^{+0.10}_{-0.11}$	8.19	$1.71^{+0.09}_{-0.06}$
1141389	NEb_1	150.386844	2.501921	23.59	3.1309	1	$10.69^{+0.04}_{-0.05}$	8.16	$1.28^{+0.10}_{-0.11}$
1157543	K1, K2, K3	150.452418	2.517077	23.04	3.1375	1	$10.64^{+0.07}_{-0.05}$	8.32	$1.69^{+0.06}_{-0.03}$
1149910	NEb_1	150.473038	2.509806	23.30	3.1133	1	$10.58^{+0.08}_{-0.06}$	8.53	$1.47^{+0.07}_{-0.08}$
1167805	K1	150.436593	2.527850	23.17	3.1086	1	$10.50^{+0.20}_{-0.15}$	8.33	$1.65^{+0.14}_{-0.12}$
1136493	NEb_1	150.393626	2.495985	22.30	3.1298	1	$10.49^{+0.12}_{-0.14}$	7.91	$1.99^{+0.02}_{-0.02}$
1168149	NEb_1	150.429878	2.525955	22.13	3.1107	1	$10.38^{+0.14}_{-0.04}$	8.08	$1.87^{+0.02}_{-0.03}$
1201047	K1	150.488328	2.558689	23.06	3.1137	1	$10.36^{+0.11}_{-0.13}$	8.05	$1.68^{+0.13}_{-0.10}$
1202406	K2	150.473857	2.559234	21.98	3.1228	2	$10.33^{+0.01}_{-0.01}$	8.09	$1.81^{+0.01}_{-0.01}$
1168871	K1	150.448872	2.529106	23.95	3.1139	1	$10.31^{+0.15}_{-0.23}$	8.08	$1.87^{+0.14}_{-0.12}$
1174559	NEb_1	150.405757	2.533855	22.99	3.1124	1	$10.27^{+0.12}_{-0.20}$	8.03	$1.58^{+0.07}_{-0.07}$
1147901	K1, K2, K3	150.427728	2.505646	21.86	3.1390	1	$10.27^{+0.01}_{-0.01}$	8.05	$1.86^{+0.02}_{-0.02}$
1158478	NEb_1	150.477543	2.518978	24.48	3.1159	2	$10.25^{+0.27}_{-0.34}$	8.23	$0.85^{+0.05}_{-0.08}$
1157402	K1	150.428193	2.517965	23.69	3.1117	1	$10.23^{+0.07}_{-0.10}$	8.43	$0.92^{+0.08}_{-0.10}$
1144934	NEb_1	150.466999	2.504471	22.88	3.1062	2	$10.23^{+0.15}_{-0.15}$	7.99	$1.76^{+0.07}_{-0.09}$
1171631	NEb_1	150.466048	2.531592	24.25	3.1141	1	$10.12^{+0.03}_{-0.05}$	8.10	$0.75^{+0.03}_{-0.02}$
1184228	K1	150.500627	2.543513	23.96	3.1485	2	$10.09^{+0.21}_{-0.15}$	8.38	$1.07^{+0.18}_{-0.07}$
1136001	NEb_1	150.399345	2.496187	24.47	3.1307	3	$10.02^{+0.09}_{-0.18}$	7.64	$0.85^{+0.09}_{-0.08}$
1155128	K1	150.440446	2.515600	23.40	3.1393	1	$9.94^{+0.02}_{-0.04}$	8.34	$1.16^{+0.05}_{-0.06}$
1142293	NEb_1	150.382452	2.502780	24.74	3.1301	2	$9.92^{+0.07}_{-0.09}$	7.93	$0.58^{+0.03}_{-0.04}$
1149534	NEb_1	150.387066	2.510379	24.55	3.1326	2	$9.91^{+0.13}_{-0.04}$	8.49	$0.93^{+0.03}_{-0.04}$
1159325	K1	150.431648	2.520075	24.56	3.1128	1	$9.84^{+0.10}_{-0.11}$	8.17	$1.11^{+0.05}_{-0.06}$
1222185	K3	150.422270	2.575857	21.96	3.1537	1	$9.29^{+0.01}_{-0.01}$	7.31	$1.35^{+0.01}_{-0.01}$
1147528	NEb_1	150.393088	2.508726	24.86	3.1126	1	$9.15^{+0.29}_{-0.16}$	8.20	$0.38^{+0.10}_{-0.07}$
1156077	NEb_1	150.432665	2.517343	24.75	3.1493	1	$8.90^{+0.10}_{-0.07}$	7.62	$0.83^{+0.09}_{-0.11}$
1179587	K1	150.454572	2.539359	24.54	3.0851	1	$8.70^{+0.01}_{-0.02}$	7.31	$0.76^{+0.01}_{-0.02}$

Notes.
[a] For all galaxies for which a spectroscopic redshift was secured, the systematic uncertainty dwarfs the statistical uncertainty. Therefore, the uncertainty on the spectroscopic redshift is taken to be the systematic uncertainty ($\delta z = 0.0012$) for each galaxy.
[b] The spectroscopic redshift confidence level was assigned based on the number of emission lines observed and their strengths. A spectrum where two emission lines were visible, e.g., Hβ and one or both lines of the [O III]$\lambda\lambda$4959, 5007 doublet, were assigned a confidence level of 1; a spectrum where a single high-S/N emission line was detected (in every case here, [O III]λ5007) was assigned a confidence level of 2; and a spectrum with a redshift fit to low-S/N emission lines was assigned a confidence level of 3.

in the inset of Figure 3). Targets for this mask were selected from the CLASSIC C2020 catalog based on their photometric redshift probability distributions $p(z)$, stellar masses, and rest-frame colors (B. Forrest et al. 2024).

We began reduction by running the MOSDEF 2D Reduction Pipeline (M. Kriek et al. 2015) to obtain 2D target and error spectra.[16] The pipeline performs a sky subtraction, masks bad pixels and cosmic rays, rectifies the slits, stacks the science exposures, and performs a telluric correction.

For the data from masks K1, K2, and K3, we extracted the 1D spectra with a Python script following the optimal K. Horne (1986) extraction. By visually inspecting the 2D spectrum, we determined whether stellar continuum or an emission feature was present. When stellar continuum was present, we collapsed the 2D spectrum along the wavelength axis to identify the location of the trace. When only an emission feature was present, we collapsed the spectrum along the limited portion of wavelength space containing the emission feature, avoiding nearby sky lines. A Gaussian was then fit to the collapsed 1D spatial emission distribution and used to weight pixels when summing the 2D spectrum along the spatial axis to produce the optimally extracted 1D spectrum and noise spectrum (K. Horne 1986). For objects that appeared in multiple masks, we weighted the extracted 1D spectra and the noise spectra by the inverse variance and coadded them. The C3VO team reduced the data from mask Neb_1 by the same process and provided the reduced 1D and 2D spectroscopic data products for galaxies with $3.1 < z < 3.2$ to the MAGAZ3NE team.

3.2. Redshift Determination

In order to obtain spectroscopic redshifts we utilized the software `slinefit`, which fits spectra with a variety of Gaussian emission and absorption features to produce best-fit redshifts and errors.[17] For an emission-line galaxy at $3 \lesssim z \lesssim 3.7$, H$\beta$ and the [O III]$\lambda\lambda$4959, 5007 doublet fall in the observed K band, so these were the primary emission features used to calculate redshifts. We obtained spectroscopic

[16] https://mosdef.astro.berkeley.edu/for-scientists/mosdef-data-reduction-pipeline/

[17] https://github.com/cschreib/slinefit

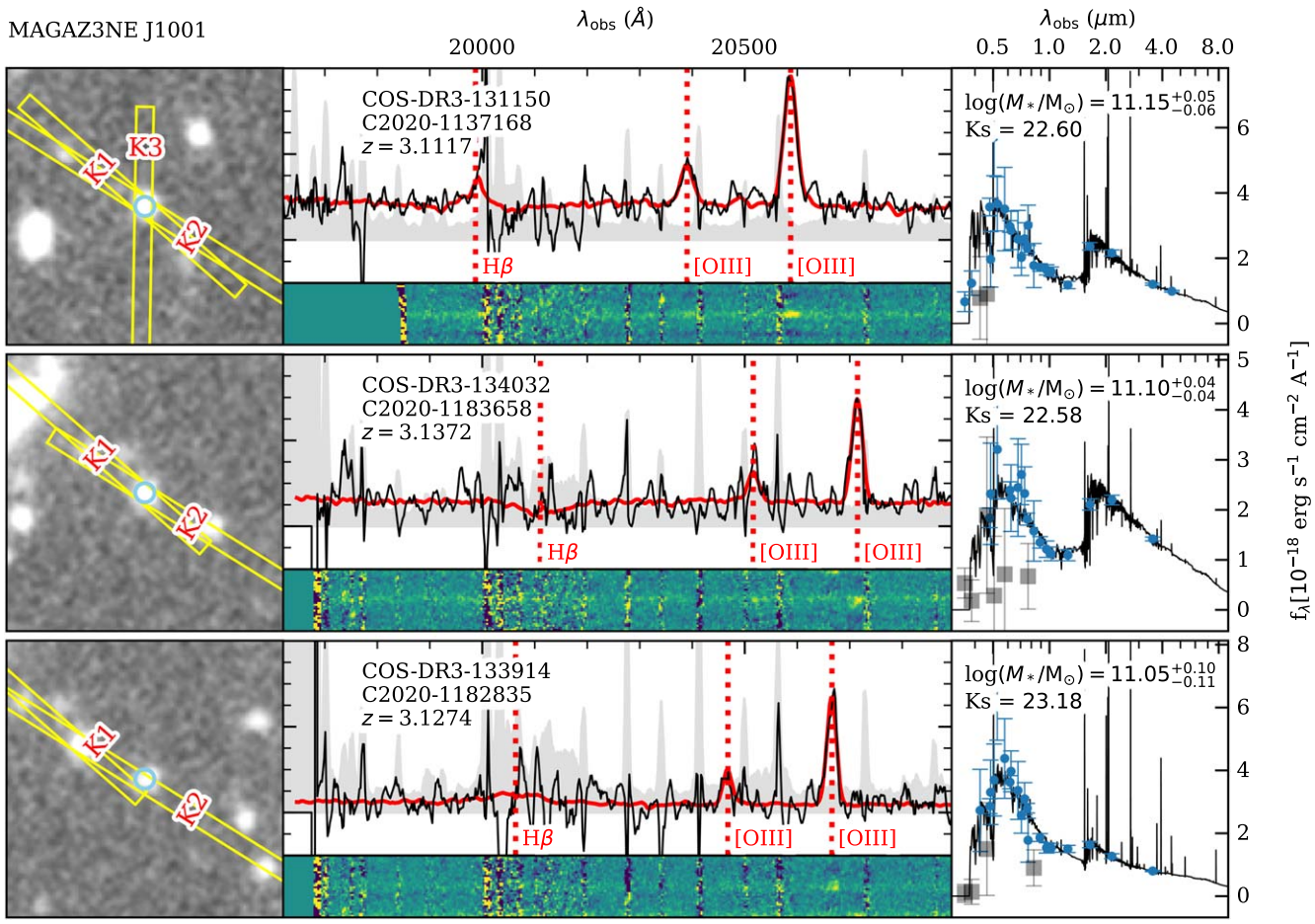

Figure 1. UltraVISTA Data Release 4 K_s-band image with overlaid MOSFIRE slit positions (left), MOSFIRE 1D K-band spectra (upper center), MOSFIRE 2D K-band spectra (lower center) and the SED (right) of the three most massive spectroscopically confirmed members (the UMGs, the first three members of Table 3, are shown here; for all spectroscopic members see Figure 4). The yellow bars indicate the slit positions on the sky and the red text indicates the mask name. The black solid line shows the spectrum smoothed over 5 pixels weighted by the inverse variance. The light gray line shows the magnitude of the error spectrum. The solid red line is the best-fit `slinefit` model. The vertical red dotted lines show the position at which Hβ and [O III]$\lambda\lambda$4959, 5007 doublet emission lines would appear at the spectroscopic redshift of each galaxy. The photometric fluxes and their 1σ errors are shown on the right in blue, with the best-fit SED shown in black. For those bands for which the signal-to-noise ratio (S/N) < 2, fluxes are shown as translucent black squares with their 1σ errors.

redshifts for 15 galaxies with $3.0 < z < 3.2$ on masks K1-3 and 13 galaxies on mask NEb_1.

Figure 1 shows the K_s-band images (left), 2D and 1D K-band spectra (center), and SEDs (right) for the three UMGs (the first three galaxies in Table 3, for all members see Figure 4). The black solid line shows the 1D spectrum smoothed over five pixels (∼11 Å), weighted by the inverse variance. The light gray line shows the error spectrum. The solid red line is the best-fit template fit output by `slinefit`, while the dotted red vertical lines show the wavelengths corresponding to Hβ and [O III]$\lambda\lambda$4959, 5007 at the best-fit spectroscopic redshift, z_{spec}.

The uncertainty on each spectroscopic redshift was obtained by adding statistical and systematic uncertainties in quadrature. Statistical uncertainties in redshift were produced by `slinefit` using 200 Monte Carlo realizations. The systematic error on the redshift was calculated by multiplying the spectral dispersion (2.17 Å pixel^{-1}) by the pixel resolution (2.78 pixels), to obtain the spectral resolution (6.03 Å). At $z \sim 3.1$, this spectral resolution corresponds to $\delta z \sim 0.0012$. In every case, the systematic uncertainty dwarfed the statistical uncertainty.

The left panel of Figure 2 shows the generally good agreement between the MAGAZ3NE spectroscopic and C2020 photometric redshifts. Three bright, low-mass spectroscopically confirmed galaxies have inconsistent photometric redshifts ($z < 1$) due to `EazyPy`'s apparent magnitude prior (which assigns low probabilities to high-redshift solutions for bright galaxies) and misidentification of the Lyman break as the Balmer break. The black circles show the 28 galaxies with spectroscopic redshifts $3.0 < z < 3.2$ (see Section 3.3). Members with broader photometric redshift probability distributions have larger photometric redshift uncertainties. We use the normalized median absolute deviation $\sigma_{NMAD} = 1.48 \times \mathrm{MAD}\,|z_{phot} - z_{spec}|/(1 + z_{spec})$ to quantify the scatter in photometric redshifts. We find that for the spectroscopic members, $\sigma_{NMAD} = 0.0331$.

In order to derive more accurate estimates of stellar mass, SFR, and age for each of the 28 galaxies shown in Table 3, we fixed $z = z_{spec}$ and then reran `EazyPy` (G. B. Brammer et al. 2008) on these galaxies in the C2020 catalog. Galaxies with stellar mass in excess of $\log(M_\star/M_\odot) > 11$ are identified with open stars in Figure 2.

3.3. Spectroscopic Members

Following the discovery of this spectroscopic overdensity around three UMGs, we iteratively run the biweight location estimator (T. C. Beers et al. 1990) on the redshifts of the 28

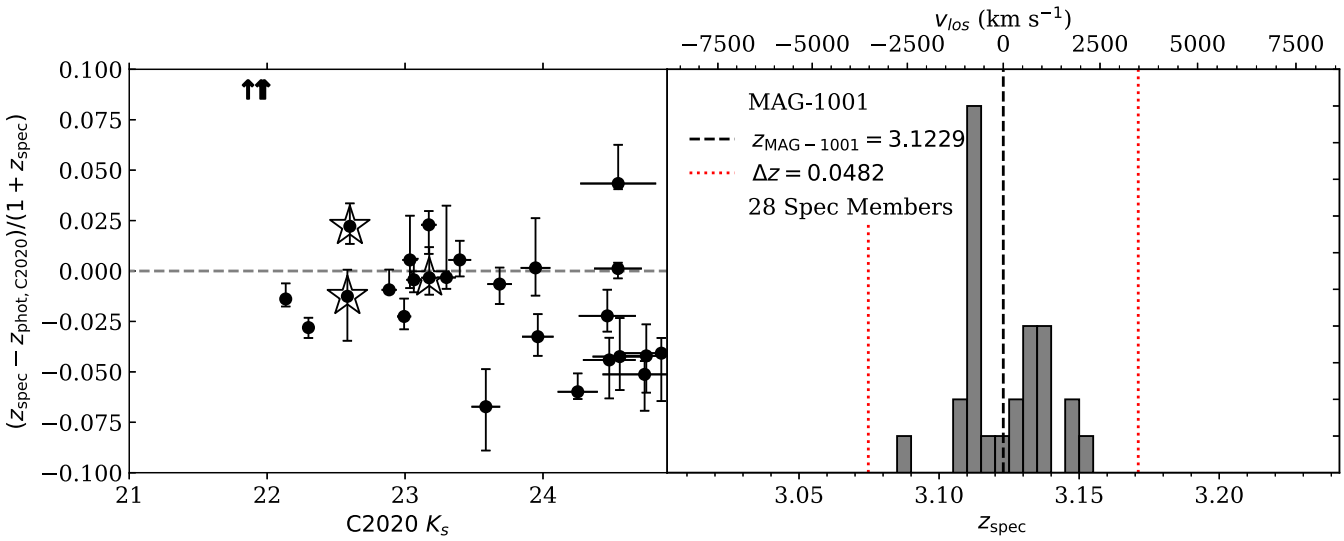

Figure 2. Left: the 28 spectroscopic members of protocluster MAG-1001 as a function of their photometric redshifts and K_s magnitudes from the C2020 catalog. Galaxies with stellar mass in excess of $\log(M_\star/M_\odot) = 11$ are marked with open stars. There is excellent agreement between the spectroscopic and photometric redshifts for the spectroscopic members (members with broader photometric redshift probability distributions have larger photometric redshift uncertainties). Three bright spectroscopically confirmed galaxies (C2020-1147901, C2020-1222185, and C2020-1202406 none with $\log(M_\star/M_\odot) > 10.5$) have a best-fit $z_{phot} < 1$ and lie outside the bounds of the plot, indicated by upward-pointing arrows. These targets were selected from the DR3 catalogs (in which they had $z_{phot} \sim 3.1$) and not C2020. Right: the histogram of the spectroscopic redshifts obtained. We calculated the protocluster redshift (dashed black line) by taking the biweight center of the 28 galaxies with velocities within ± 6000 km s^{-1} ($\Delta z = 0.08$) of the most massive UMG, C2020-1137168. The dashed red lines show the $3 \times \sigma_z$ limits for spectroscopic membership. All 28 galaxies meet this membership selection criterion. Those galaxies are indicated by magenta crosses in Figure 3 and their properties are summarized in Table 3).

galaxies with line-of-sight velocities within ± 6000 km s^{-1} ($\Delta z = 0.08$) of the most massive galaxy, C2020-1137168, to determine the central redshift. In the first iteration, we use the distribution of redshifts and the statistical median as input values; for iteration N ($N > 1$), the estimated center from iteration $N - 1$ is input as the distribution median value (instead of using the actual statistical median of the distribution). We run five iterations, but the central redshift rapidly converges to $z = 3.122^{+0.007}_{-0.004}$. The biweight scale was found to be $\sigma_z = 0.0161^{+0.0012}_{-0.0038}$. The uncertainties on the biweight center and scale were calculated using bootstrapping.

The right panel of Figure 2 shows a histogram of the redshifts for members of the spectroscopic overdensity, which we define to be galaxies with spectroscopic redshifts within three times the biweight scale width of the central redshift (similar to, e.g., T. Yuan et al. 2014; B. Darvish et al. 2020). The central redshift is shown by the dashed black line and the $3 \times \sigma_z$ limits are shown by the dashed red lines. There are 28 spectroscopic members of the overdensity, which we name protocluster MAGAZ3NE J100143+023021 (hereafter MAG-1001).

We adopt the naming convention for protoclusters as utilized by McC22, with the R.A. (α) and decl. (δ) of the system chosen to coincide with the coordinates of the most-massive, spectroscopically confirmed member (C2020-1137168; choosing either of the other two UMGs as the protocluster "center" yields consistent results in our analyses). A previous study of photometric galaxy overdensities in the COSMOS field using the UltraVISTA DR1 catalog identified a number of protocluster candidates at $1.6 < z < 3.1$ (Y.-K. Chiang et al. 2014). The highest redshift (and highest overdensity) candidate was identified at $z = 3.08$ with a sky position of $\alpha = 150\overset{\circ}{.}293$ and $\delta = 2\overset{\circ}{.}507$. The proximity on the sky and in redshift leads us to conclude that these are likely the same structures. MAG-1001 also coincides with one of the $z \sim 3.1$ Lyα blob and Lyα emitter (LAE) overdensities (the west portion of "Complex A"), at the junction of several cosmic filaments, independently identified in V. Ramakrishnan et al. (2023) from the ODIN survey. While MAG-1001's sky position has significant overlap with the "S6" substructure in Elentári protosupercluster (B. Forrest et al. 2023), the 20 spectroscopically confirmed members of S6 at $z \sim 3.33$ confirms that it is a separate structure from MAG-1001.

The positions of the 28 spectroscopic protocluster members are shown by magenta crosses in Figure 3, with the three spectroscopically confirmed UMGs marked by blue stars.

4. Protocluster Membership

4.1. Photometric Redshift Selection

In order to determine photometric membership for each protocluster, we utilize the best-fit photometric redshifts and stellar masses output by `EazyPy`. There are 1,720,700 objects in the CLASSIC C2020 catalog, 959,216 of which lie within the UltraVISTA survey footprint. To map the COSMOS field and protocluster environments, we selected bright and massive galaxies at $z \sim 3$ ($K_s \leqslant 24.5$, $\log(M_\star/M_\odot) \geqslant 10.5$, and $2.25 < z_{peak} < 4$) from the UltraVISTA footprint. There were 12,395 galaxies that satisfied those three criteria.

To more precisely select galaxies at similar redshift to each protocluster, we utilize the method from McC22. To briefly summarize, we perform a probabilistic selection to account for a wide range of photometric uncertainties. For each protocluster, we integrated $p(z)$ for each galaxy using the protocluster redshift as the fiducial central redshift and the median photometric uncertainty of the sample of 12,395

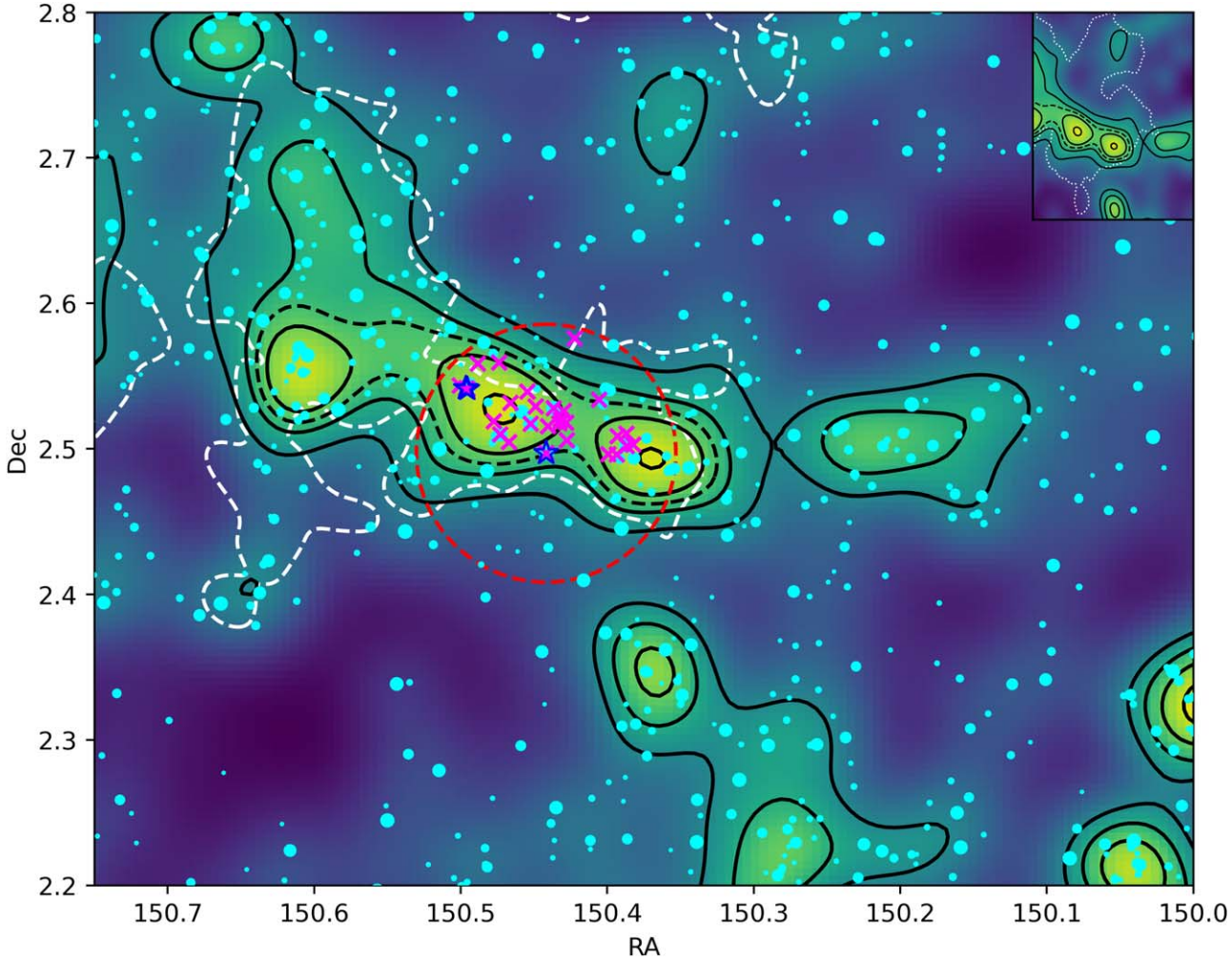

Figure 3. Gaussian kernel density map of galaxies in the COSMOS2020 catalog (cyan circles) after photometric redshift, stellar mass, K_s-band magnitude, and probability cuts described in Section 4.1 have been applied at $z = 3.125$. The size of each galaxy's cyan circle is scaled by its P value. Spectroscopically confirmed protocluster members are shown as magenta crosses and the three spectroscopically confirmed UMGs are denoted by open blue stars (the markers for C2020-1182835 and C2020-1183658 overlap on the top left). The solid black contour lines indicate the 1σ, 2σ, etc. levels of the density distribution and the dashed black 2.5σ contour line shows the structure "core" region (see Section 6.1.1). The red dashed circle (with a projected radius of 10 comoving Mpc) centered on the most massive UMG, C2020-1137168, indicates the region from which protocluster member galaxies were selected. The coeval "field" sample is comprised of the galaxies that fall outside both the 1σ density contours and the 10 cMpc radius circle centered on the most massive UMG. The white dashed line shows the 3σ overdensity contour of $z \sim 3.1$ LAEs from V. Ramakrishnan et al. (2023). For comparison, the 2σ overdensity limits of the $z = 3.3$ structure Elentári S6 is shown as a white dotted contour in the inset in the top right with the KDE and contours.

galaxies, $\Delta z_{\text{phot, sample}}$, as the lower and upper limits.

$$P = \frac{\int_{z_{\text{PC}}-\Delta z_{\text{phot, sample}}}^{z_{\text{PC}}+\Delta z_{\text{phot, sample}}} p(z)dz}{\int_0^{\infty} p(z)dz}. \quad (1)$$

Galaxies with an integrated probability P in excess of a threshold probability P_{thresh} will be considered members of the protocluster redshift slice. The values of $\Delta z_{\text{phot, sample}}$ and P_{thresh} were found to be $\Delta z_{\text{phot, sample}} = 0.0213(1 + z_{\text{PC}})$ and $P_{\text{thresh}} = 0.17$, following the method set out in McC22 and briefly explained below.

In the C2020 catalog for the selection of 12,395 galaxies described above, the median uncertainty on photometric redshifts is $\Delta z_{\text{phot, sample}}/(1 + z_{\text{phot}}) = 0.0213$, which we then use to calculate the integrated probability P for each galaxy at a given protocluster's redshift using Equation (1).

To determine the threshold value, P_{thresh}, we consider a hypothetical "worst-case scenario" member galaxy, which has a Gaussian $p(z)$ with an uncertainty of three times the median photometric redshift uncertainty, $\Delta z_{\text{phot, sample}}$ (this corresponds to the 90th percentile of $\Delta z/(1 + z_{\text{phot}})$ values). We would like this galaxy to fall just at the P_{thresh} limit for inclusion in the redshift slice. To achieve this we set the photometric redshift of this hypothetical galaxy such that the redshift of the galaxy's protocluster fell at this galaxy's photometric redshift uncertainty (i.e., $z_{\text{phot}} \pm \Delta z_{\text{phot, galaxy}} = z_{\text{PC}}$). By applying Equation (1) to this hypothetical galaxy, we obtained $P = 0.17$, which we then adopt to be the threshold probability P_{thresh}. Each of the 12,395 galaxies in our sample with $P \geqslant P_{\text{thresh}}$ are considered to be members of the given protocluster's redshift slice.

To test the robustness of our analyses to this P-based photometric selection criteria, we consider two additional P cutoff values for "high" and "moderate" quality photometric members, determined similarly to P_{thresh}. The P for "moderate" and "high" probability membership was determined by considering a hypothetical galaxy with a Gaussian $p(z)$ distribution, but with an uncertainty equal to the median photometric uncertainty. For "high" probability members, we set z_{phot} at

the redshift of the protocluster z_{PC}, which produces $P = 0.68$ using Equation (1) (i.e., a Gaussian integrated between its 1σ limits). For "moderate" probability membership, we adopt a z_{phot} placement such that the redshift of the protocluster falls at the 1σ uncertainty of the galaxy's $p(z)$ distribution (as was done for P_{thresh}; $z_{phot} \pm \Delta z_{phot,\ galaxy} = z_{PC}$). Applying Equation (1) to a hypothetical galaxy with this $p(z)$ and placement gives $P = 0.48$. We adopt these values to be $P_{high} = 0.68$ and $P_{mod} = 0.48$ for assessing membership quality, and use P_{thresh} as the fiducial minimum for consideration.

Finally, we automatically include galaxies in a protocluster's redshift slice based on spectroscopic redshifts, with spectroscopically confirmed members assigned $P = 1$. For pairs of protoclusters close in redshift (i.e., MAG-0959 and MAG-1000, RO-1001 and VPC-1000), spectroscopic members are all assigned $P = 1$ when either structure's redshift slice is considered.

To generate galaxy density maps of the COSMOS field at each protocluster redshift, we apply a Gaussian kernel density (KDE) estimator to the members of each redshift slice, weighted by the galaxies' P values. To determine the bandwidth (i.e., the standard deviation of the Gaussian kernel), we maximize the likelihood cross-validation (P. HALL 1982; see also N. Chartab et al. 2020 for an in-depth discussion of its astrophysical application) in the range of $0\farcm06$ to $12'$ in 50 steps.

4.1.1. MAG-1001

We show the smoothed density map for MAG-1001 and the COSMOS field at $z = 3.125$ in Figure 3, with maximal density colored yellow, and solid black contours drawn at the 1σ, 2σ, etc. values of the density distribution. The cyan circles show the 2372 galaxies that have $P \geqslant 0.17$, each with its size scaled by its P value. We find that the optimized bandwidth for the selected galaxies presented here is $1.'68$, corresponding to roughly 3.15 comoving Mpc. We show the 3σ overdensity contour from the Voronoi tesselation of $z \sim 3.1$ LAEs from in V. Ramakrishnan et al. (2023) as a white dashed line in Figure 3. We also indicate the outline of the S6 region with a dotted white contour in the inset of Figure 3. We compare our results with these other structures in Section 6.1 and estimate the extended overdensity's mass in Section 6.1.1.

Another photometric overdensity is located at $\alpha \sim 149\fdg95$ and $\delta \sim 2\fdg35$ (the corner of which is visible in Figure 3). Despite the high-density signal, this structure is not detected in the ODIN Lyα map, which indicates it may lie at a lower or higher redshift. To investigate, we performed the photometric redshift selection between $z = 2.9$ and 3.3 in $\delta z = 0.01$ steps and found that this structure's photometric overdensity signal is highest at $z \sim 3.05$. A moderate overdensity in this region is also detected in combined VUDS spectroscopy and photometry (D. Hung et al. 2024).

4.2. Central UMG Selection

We select the most massive spectroscopically confirmed UMG to be the "central" UMG of a given protocluster. In protocluster VPC-1000 (for which member galaxy redshifts have not been published; O. Cucciati et al. 2014), we select the most massive photometric UMG with $P > 0.68$ within the highest density contour to be the fiducial central UMG. We note that in this protocluster, all photometric UMGs are *UVJ* star-forming (Section 5.1). The C2020 ID for the selected central UMG of each protocluster is listed in Table 1.

Simulations have shown that at $z \sim 3$, 10 comoving Mpc is approximately equal to the radius at which the membership probability drops to 50% (Y.-K. Chiang et al. 2017). As a final step in determining a central UMG's environment and generic "protocluster region," we select only those galaxies within a radius of 10 comoving Mpc from the central UMG. We define all galaxies in the redshift slice that fall within this radius to be "protocluster members" (including the central UMG). To produce the coeval field sample, we select from the redshift slice's galaxies with $P \geqslant P_{thresh}$ all of the galaxies that lie outside both the 1σ density contours in the overdensity map and the 10 cMpc radius circle around the central UMG.

In MAG-1001, this selection resulted in a total of 58 photometric members for MAG-1001 (seven of these galaxies are spectroscopic members, so the total number of photometric, nonspectroscopic members is 51; see Table 4 membership assuming different threshold values and for other protoclusters). We note that most spectroscopically confirmed members of the protocluster have stellar masses below the photometric mass selection limit applied to the photometric catalog (Table 3). As a result, these galaxies were not identified as photometric members despite otherwise having photometric redshifts consistent with membership.

5. *UVJ* Classification and Quiescent Fractions

5.1. Rest-frame Colors and UVJ Classification

The *UVJ* diagram has become an established method for separating quiescent from star-forming galaxies (S. Wuyts et al. 2007; R. J. Williams et al. 2009). Rest-frame $U - V$ and $V - J$ colors were calculated from the best-fit SED models of the spectroscopic members of each COSMOS protocluster output by `EazyPy` (G. B. Brammer et al. 2008) with the C2020 template sets having set $z = z_{spec}$. Uncertainties for these colors were calculated by propagating the uncertainties on the rest-frame U, V, and J fluxes from `EazyPy`. The $U - V$ and $V - J$ colors for photometric members are taken from the C2020 catalog. $U - V$ and $V - J$ colors for galaxies in MAG-0959 and 1000 calculated using the C2020 catalog and templates are generally consistent with those derived from the UltraVISTA DR3 catalog in McC22.

Figure 5 shows rest-frame $U - V$ and $V - J$ colors for members of the MAG-1001 system. The three UMGs are highlighted as black stars and the 25 other spectroscopically confirmed members of MAG-1001 with $M_\star \geqslant 10^{10.5}\,M_\odot$ ($M_\star < 10^{10.5}\,M_\odot$) are shown as solid (open) black squares. The shaded blue circles show the 51 galaxies classified as photometric members of MAG-1001, with the shading corresponding to the probability (P) of membership for each galaxy (see Section 4.1).

Also plotted in Figure 5 is the quiescent selection criteria proposed by K. E. Whitaker et al. (2011). All spectroscopically confirmed galaxies are *UVJ* star-forming, including the three UMGs and four other galaxies with stellar mass $\log(M_\star/M_\odot) \geqslant 10.5$, as are the majority of photometric members. One photometric member with $\log(M_\star/M_\odot) \gtrsim 11$ and $P > 0.68$ falls into the *UVJ*-quiescent bin and features a post-starburst best-fit SED, though it falls in the UltraVISTA deep region (and is thus not included in the ultradeep UltraVISTA DR3 catalog and was not considered for spectroscopic target selection on masks K1-3).

Table 4
COSMOS Protocluster Quiescent Fractions

Protocluster ID	z_{PC}	P_{thresh} (%, corrected)	Protocluster QF (%)	Field QF #	Protocluster Q/SF #	Field Q/SF
QO-1000	2.77	$P \geqslant 0.17$	$41.4^{+16.6}_{-14.2}$	$8.3^{+1.4}_{-0.3}$	14/62	232/2520
		$P \geqslant 0.48$	$45.9^{+12.5}_{-18.3}$	$8.1^{+1.7}_{-0.6}$	7/25	93/998
		$P \geqslant 0.68$	$38.0^{+21.4}_{-10.0}$à	$7.4^{+1.8}_{-0.8}$	3/12	44/528
VPC-1000	2.90	$P \geqslant 0.17$	$8.8^{+5.6}_{-8.8}$	$6.3^{+2.1}_{-0.9}$	6/59	187/2388
		$P \geqslant 0.48$	$5.5^{+10.2}_{-5.5}$	$4.7^{+3.0}_{-1.8}$	1/22	44/785
		$P \geqslant 0.68$	$16.3^{+0.4}_{-16.3}$	$2.1^{+6.0}_{-2.1}$	1/10	8/354
RO-1001	2.91	$P \geqslant 0.17$	$13.5^{+10.0}_{-9.0}$	$5.8^{+1.9}_{-0.7}$	9/70	171/2369
		$P \geqslant 0.48$	$6.5^{+17.7}_{-1.5}$	$3.8^{+3.3}_{-2.1}$	1/24	36/822
		$P \geqslant 0.68$	$8.6^{+15.1}_{-4.0}$	$2.6^{+4.8}_{-2.6}$	1/17	11/384
MAG-1001	3.12	$P \geqslant 0.17$	$6.3^{+6.2}_{-3.9}$	$4.0^{+2.6}_{-0.9}$	5/53	57/1040
		$P \geqslant 0.48$	$3.5^{+9.3}_{-0.9}$	$2.5^{+3.4}_{-1.9}$	1/29	10/372
		$P \geqslant 0.68$	$5.1^{+7.4}_{-2.5}$	$2.3^{+3.7}_{-2.1}$	1/17	5/181
MAG-0959[a]	3.37	$P \geqslant 0.17$	$17.6^{+9.7}_{-4.7}$	$3.8^{+3.0}_{-2.2}$	6/36	20/426
		$P \geqslant 0.48$	$18.3^{+9.0}_{-5.4}$	$3.0^{+5.3}_{-2.3}$	4/20	5/138
		$P \geqslant 0.68$	$15.9^{+11.4}_{-3.1}$	$0.0^{+8.9}$	2/13	0/51[b]
MAG-1000	3.38	$P \geqslant 0.17$	$6.2^{+7.4}_{-6.2}$	$3.9^{+2.9}_{-2.3}$	1/15	20/425
		$P \geqslant 0.48$	$7.9^{+5.4}_{-7.9}$	$3.0^{+5.3}_{-2.4}$	1/9	5/136
		$P \geqslant 0.68$	$0.0^{+12.9}$	$0.0^{+8.7}$	0/6[b]	0/46[b]

Notes.
[a] In this work, we calculate a quiescent fraction for galaxies with $\log(M_\star/M_\odot) \geqslant 10.5$, whereas in McC22 the quiescent fraction was also separated into different mass bins and the reported elevated quenched fraction was for galaxies with $\log(M_\star/M_\odot) \geqslant 11$.
[b] Despite no galaxies falling into the quiescent bin, we obtain a nonzero upper 1σ uncertainty on the associated QF because we resample the rest-frame U, V, and J fluxes when calculating the QF errors.

5.2. Quiescent Fractions

The quiescent fraction of a population of N galaxies can be simply expressed as

$$QF = \frac{1}{N}\sum_{i=1}^{N} q_i, \tag{2}$$

where q_i is 1 for a galaxy classified as quiescent and 0 for a galaxy classified as star-forming based on their rest-frame $U-V$ and $V-J$ colors, summed over all N galaxies in that population. Here, to account for the wide range in $p(z)$ quality (and therefore photometric redshift uncertainty), we weight each galaxy's contribution by its associated integrated P such that

$$QF = \frac{\sum P_i q_i}{\sum P_i}. \tag{3}$$

We use Equation (3) to calculate the quiescent fractions of the coeval field populations. To calculate the quiescent fraction of a given protocluster, we must also correct the number of quiescent/star-forming protocluster members by subtracting the number of field galaxies one would expect to find in an equivalent volume (both populations as defined in Section 4.2):

$$QF = \frac{\sum P_i q_i - C\sum P_j q_j}{\sum P_i - C\sum P_j}, \tag{4}$$

where protocluster members are summed over i, coeval field galaxies are summed over j, and C is the ratio of protocluster to field volume based on the regions defined in Section 4.2.

To calculate the uncertainties of these quiescent fractions, we perform a P-weighted Monte Carlo simulation and recalculate the rest-frame colors. In each of 10,000 Monte Carlo iterations, for each galaxy in the protocluster and field, we draw a random number between 0 and 1. If the P value of that galaxy exceeds the random number, its P_i or P_j is set to 1 (it is included in the redshift slice), otherwise it is set to zero (it is rejected from the redshift slice). We also account for uncertainty of each individual galaxy's rest-frame colors by also resampling the rest-frame U, V, and J fluxes. For each rest-frame band, we reassign the flux by drawing a random sample from a normal distribution centered on the model's best-fit flux with width σ equal to the uncertainty on that best-fit flux. We then reassess q_i or q_j based on these new, resampled fluxes. Protocluster and field quiescent fractions are then calculated for each iteration and we take the upper and lower 1σ limits of the QF distribution to be the uncertainty on the quiescent fractions calculated using Equations (3) and (4).

The quiescent fractions QF of the protoclusters for different values of P_{thresh} are given in Table 4 (ordered by redshift, as Table 1). We discuss our results in the context of other protoclusters with confirmed UMGs and measured quiescent fractions in the literature Section 6.2 and speculate as to which mechanisms could be responsible in Section 6.2.1.

6. Discussion

6.1. MAG-1001 and z ∼ 3.1 Large-scale Structure in COSMOS

Unlike the other protoclusters in this work (which appear spatially compact, extending ∼10–20 comoving Mpc end-to-

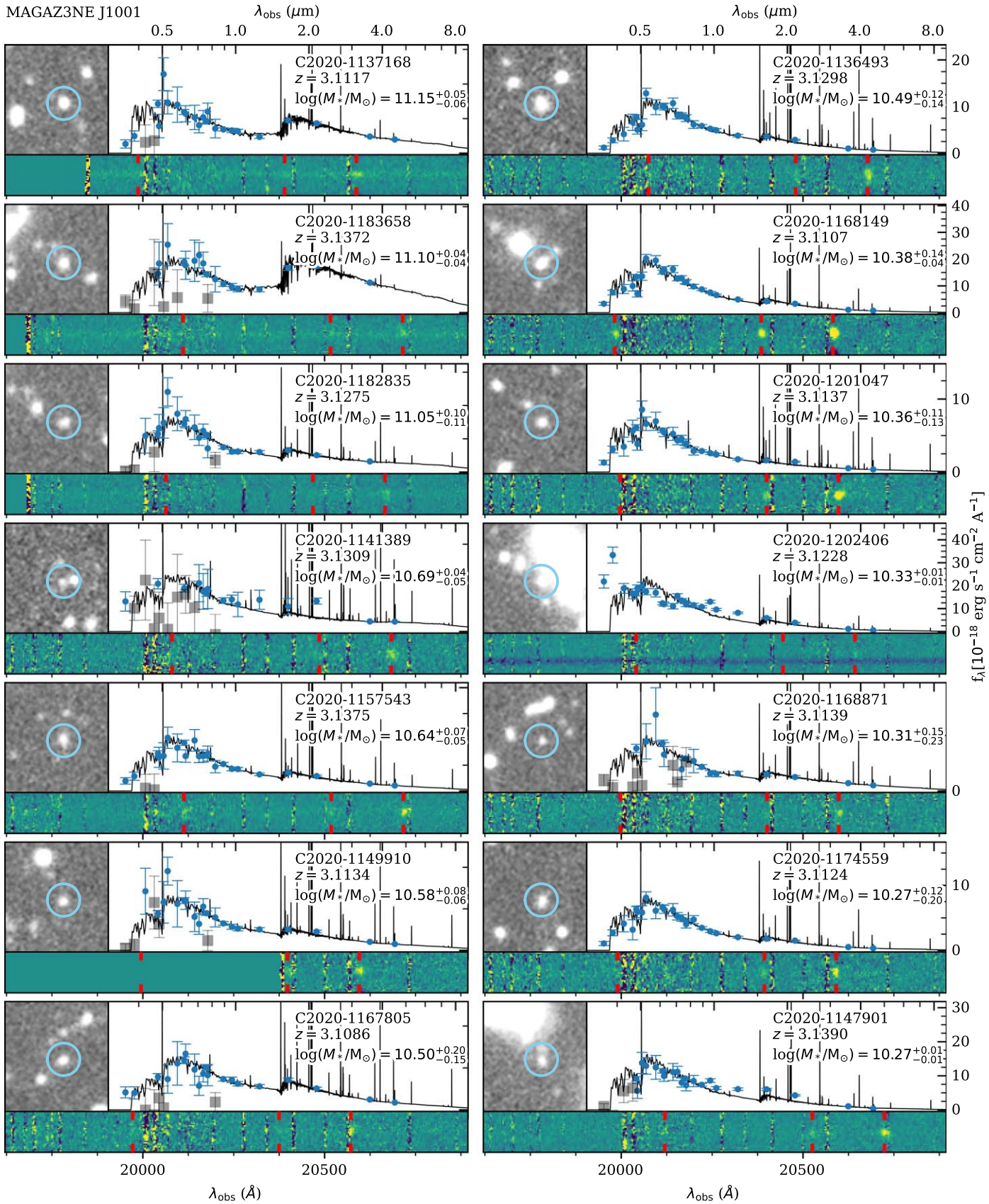

Figure 4. All 28 spectroscopic members of MAGAZ3NE J100143+023021 shown in order of decreasing mass (from to to bottom, left to right), the same order as in Table 3. Top left: target K_s-band cutout. Top right: best-fit `EazyPy` SED and photometric fluxes with 1σ errors. Bottom: 2D K-band spectrum with red lines indicating the location of observed Hβ and [O III]$\lambda\lambda$4959, 5007 wavelengths.

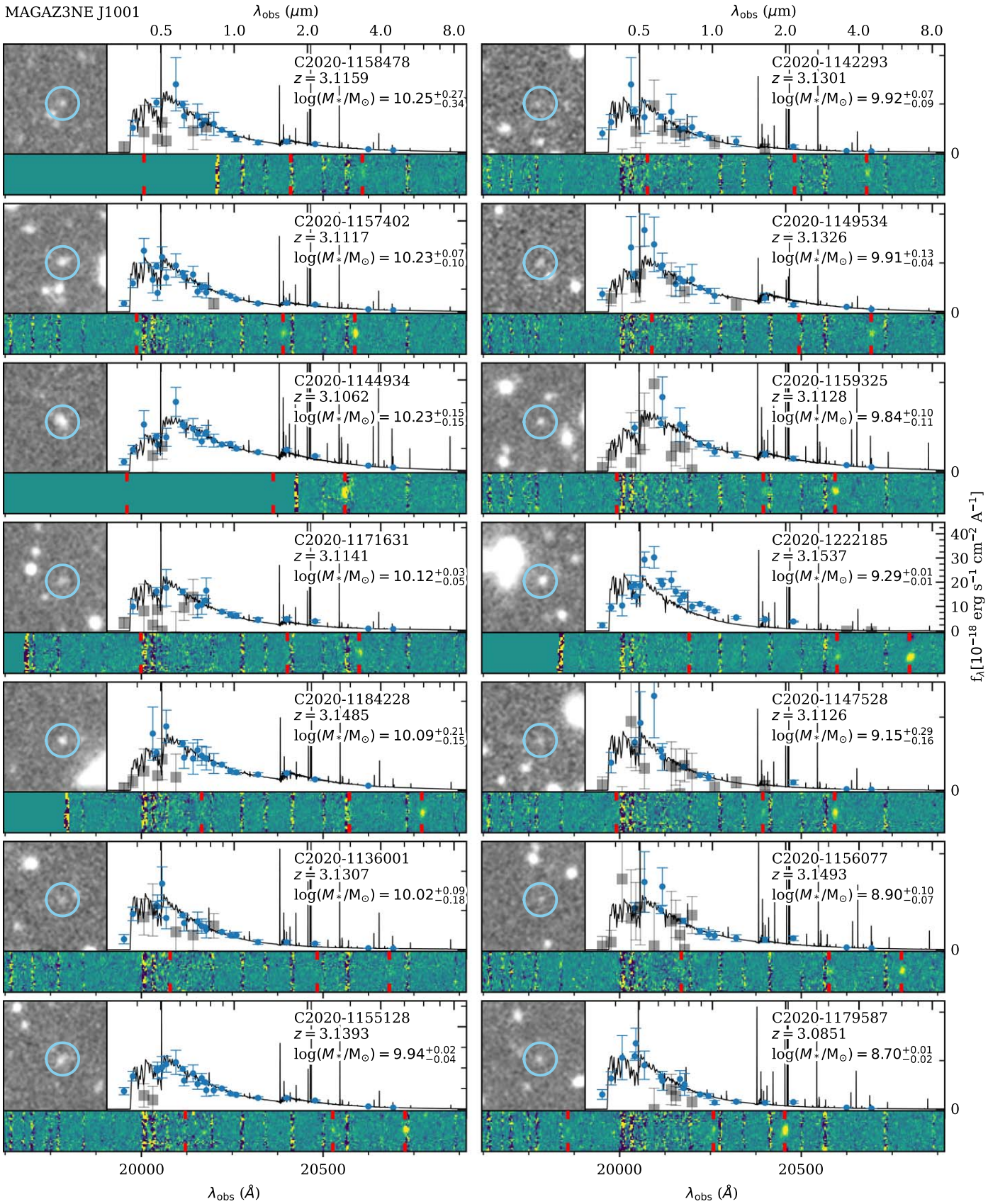

Figure 4. (Continued.)

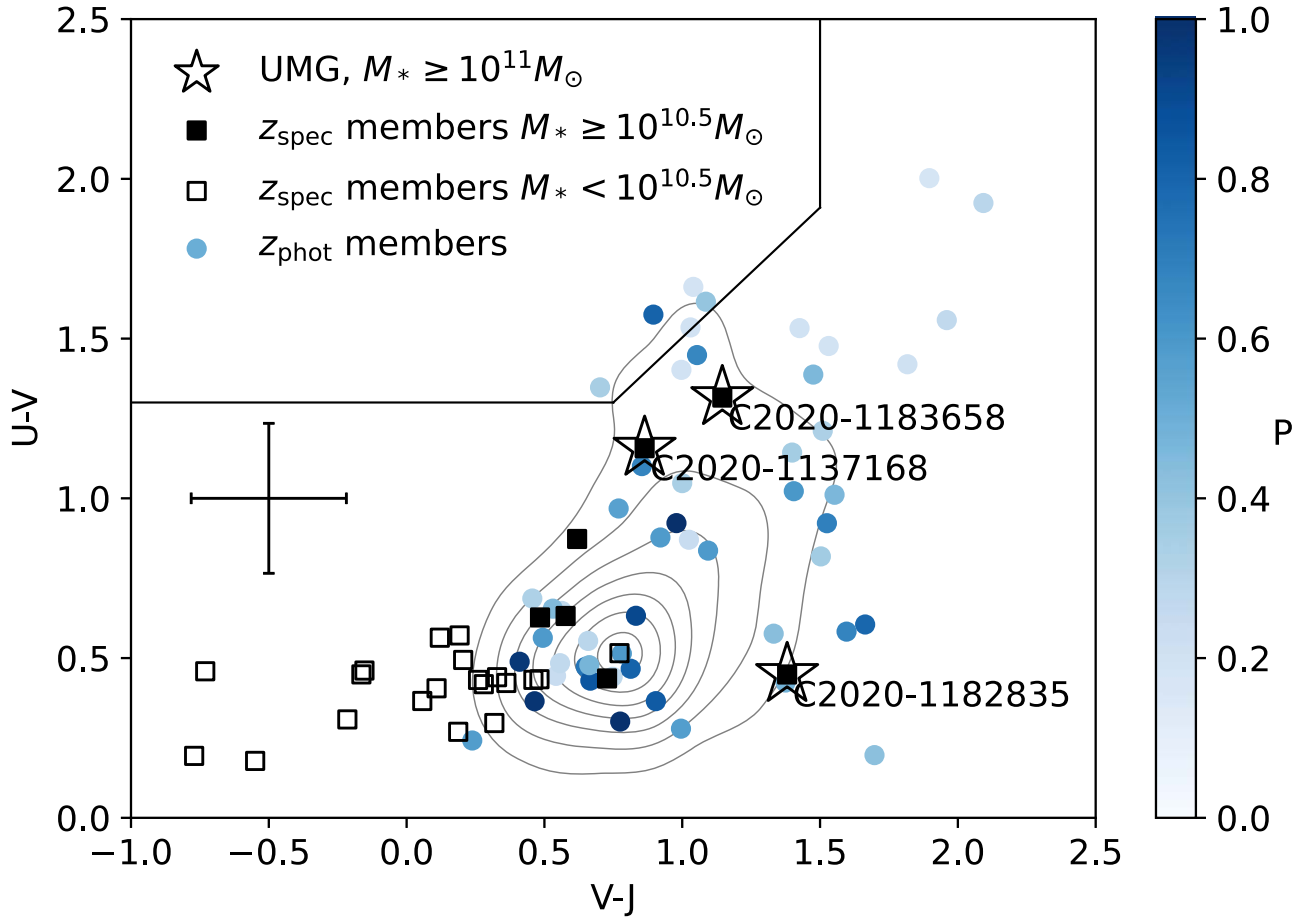

Figure 5. *UVJ* color–color diagram for MAG-1001. The 28 spectroscopic members and 51 photometric members of MAG-1001 are shown as black squares and shaded blue circles, respectively. The three open stars denote the three spectroscopically confirmed UMGs in the protocluster (their IDs are displayed nearby). Note that most of the spectroscopically confirmed members of the protocluster were not identified as photometric members because they fall below the stellar mass cut ($\log(M_\star/M_\odot) = 10.5$; open black squares) applied to the C2020 catalog. Only seven spectroscopically confirmed members have a stellar mass greater than or equal to $\log(M_\star/M_\odot) = 10.5$ (solid black squares; see Table 3), three of which are the UMGs. Each photometric member is shaded according to its P value (darker blue corresponds to a higher P as displayed in the colorbar). The contours show the field sample (defined in Section 4.2), and the wedge defined by the solid black lines shows the quiescent galaxy selection criteria proposed by K. E. Whitaker et al. (2011). The floating errorbars show the median errors on $U - V$ and $V - J$ colors for the spectroscopically confirmed members (primarily inflated by faint, low-mass members; see Table 3).

end), MAG-1001 appears to be embedded in a much physically larger photometric overdensity of massive galaxies (Figure 3).

We show the photometric overdensity of massive galaxies around MAG-1001 in Figure 3 (colored density map and black contours) and compare it with the LAE overdensity "Complex A" from the ODIN survey V. Ramakrishnan et al. (2023), the 3σ overdensity contour of which is shown as a white dashed line. As the redshifts precision of LAEs detected in narrowband surveys are several times more precise than the best-fit photometric redshifts fit to broadband filters with minimal contamination, the agreement between the massive galaxy overdensity around MAG-1001 and Complex A is a good indication that both of these overdensity maps trace the same large-scale cosmic structure. We also show the 2σ overdensity contours of the $z = 3.33$ structure S6 in Elentári (mainly detected as a photometric overdensity; B. Forrest et al. 2023) as a white dotted line in the inset of Figure 3, though these contours are less well-matched to MAG-1001 and Complex A.

In the extended MAG-1001 structure, the three aligned 3σ overdensity peaks extend 35 cMpc east-to-west from end-to-end, which is well-matched to the expected spatial extent of massive cluster progenitors from simulations (e.g., S. I. Muldrew et al. 2015). The region enclosed by the 2σ contour of the massive galaxy overdensity (which roughly matches the associated LAE overdensity) spans nearly 0.4° by 0.4° ($\sim 50 \times 50$ cMpc^2) region, which is roughly comparable to the protosuperclusters Hyperion at $z = 2.45$ (O. Cucciati et al. 2018) and S1-5 in Elentári at $z = 3.3$ (S6 is poorly constrained and likely contaminated by the $z \sim 3.1$ structure; B. Forrest et al. 2023, 2024). We speculate that this overdensity could be another such structure at $z \sim 3.1$.

Although we only focus on one spectroscopically confirmed overdensity in this structure, several other protocluster candidates have been identified in the surrounding region at this redshift (D. Hung et al. 2024; V. Ramakrishnan et al. 2024). We also note that many of the ODIN LAE overdensities in Complex A lie outside the UltraVISTA footprint (where, therefore, we cannot reliably estimate stellar masses) in a region over one square degree on the sky (V. Ramakrishnan et al. 2023). The proximity of these additional overdensities in a large region hints at potentially an even larger early cosmic structure. Further study of this region and the associated structure(s) would offer key insights into environmental effects on galaxy evolution at $z \sim 3$ and provide an important observational comparison for supercluster progenitors in large cosmological simulations.

6.1.1. Structure Overdensity and Mass

The near-uniform K_s-band coverage of the COSMOS field in the UltraVISTA Survey's Data Release 4 imaging allows us to estimate the galaxy overdensity in the region containing MAG-1001. We perform simple rough estimation of the protocluster's mass at $z = 3.12$ using the equation $M_{\rm tot} = \rho V(1 + \delta_m)$ (as in e.g., O. Cucciati et al. 2018; L. Shen et al. 2021; B. Forrest et al. 2023), where ρ is the cosmic matter density at $z = 3.12$, V is the protocluster volume, and δ_m is the matter overdensity within the protocluster volume. To find V and δ_m, we utilize the Gaussian KDE we used to produce Figure 3 in Section 4.1. First, however, we will discuss the limitations of any such estimate using photometric redshifts.

The large uncertainties associated with photometric redshifts correspond to line-of-sight distances, which are significantly greater than the typical extent of protoclusters, and thus may dilute or inflate the overdensity signal. Y.-K. Chiang et al. (2013) showed that the large Δz windows associated with photometric selections dilute protocluster overdensity signals by smoothing over the density field. A photometric redshift overdensity of $\delta_{\rm gal} \sim 1.5$ could correspond to actual overdensities of $2 \lesssim \delta_{\rm gal} \lesssim 7$. Conversely, any overlapping unassociated structure or line-of-sight filaments could lead to measurements of higher overdensity than the real values. The "S6" structure in Elentári (B. Forrest et al. 2023, 2024) at $z \sim 3.33$ overlaps with the structure around MAG-1001 (both S6 and MAG-1001 were identified as photometric and spectroscopic overdensities). While the spectroscopic overdensities confirm the existence and redshifts of these structures, it is also possible (if not likely) that S6 and MAG-1001 are contaminated by each other's photometric overdensity measurements.

With these caveats in mind, we consider the extended region with surface density greater than 2.5 times the standard deviation of the density distribution (i.e., $\Sigma > 2.5\sigma_\Sigma$, the black dotted contour in Figure 3) to comprise the structure "core," which spans 68 square arcminutes (equivalent to 240 cMpc^2). We chose this contour, which contains the continuous high-density extended east–west structure, without selecting the lower-density structure to the northeast or the overdensities south and west. As the uncertainty on photometric redshifts typically exceeds the line-of-site extent of protoclusters, we instead take the protocluster volume to be that of a cube with cross-sectional area equal to the area of the 2.5σ contour described above ($A = 240$ cMpc^2, thus $V = 3,\ 728$ cMpc^3, assuming $V = A^{3/2}$).

The median galaxy overdensity of this peak is $\delta_{\rm gal} = (\Sigma_{\rm gal} - \bar{\Sigma}_{\rm gal})/\bar{\Sigma}_{\rm gal} = 1.450^{+0.165}_{-0.029}$. We then approximate the matter overdensity from the galaxy overdensity by the galaxy bias parameter b, where $b = \delta_{\rm gal}/\delta_m$. We adopt $b = 3.5$ which is in-line with observational studies of LBG clustering at $z \sim 3$ (K. L. Adelberger et al. 1998; M. Giavalisco et al. 1998; C. C. Steidel et al. 1998) and cosmological simulations (e.g., A. Barreira et al. 2021).

To calculate the uncertainty of this mass estimate, we employ a simple Monte Carlo simulation using the P values of the photometric members and the Gaussian KDE. For each of the 250 Monte Carlo realizations, we redraw membership of the redshift "slice" based on their P values. For each galaxy, we draw a random number between 0 and 1 and if the P value of that galaxy exceeds the random number, it is considered a member of the redshift "slice." We then apply a nonweighted Gaussian KDE estimator to each realization; weighting the KDE after selecting galaxies in this manner would overbias high probability members and therefore give a higher protocluster density and mass. We combine the density measurements from all Monte Carlo realizations to obtain the median galaxy density $\bar{\Sigma}_{\rm gal}$ and the standard deviation of the galaxy density distribution σ_Σ to minimize the impact of individual realizations with atypically high/low field densities. For each realization, we calculate the overdensity and total mass of the protocluster using the method described above. We take the 16th and 84th percentile values to be the lower and upper limits of the uncertainty on the density and total mass estimates.

Table 5
MAG-1001 Structure Overdensity and Mass

	2.5σ Region		2σ Region	
$P_{\rm thresh}$	$\delta_{\rm gal}$	$M_{\rm tot}$ ($10^{14}\,M_\odot$)	$\delta_{\rm gal}$	$M_{\rm tot}$ ($10^{14}\,M_\odot$)
$P \geqslant 0.17$	$1.450^{+0.165}_{-0.029}$	$2.25^{+1.55}_{-0.65}$	$1.250^{+0.193}_{-0.005}$	$4.78^{+1.30}_{-1.53}$
$P \geqslant 0.48$	$1.429^{+0.117}_{-0.062}$	$3.58^{+1.27}_{-1.23}$	$1.317^{+0.068}_{-0.112}$	$5.73^{+1.96}_{-1.12}$
$P \geqslant 0.68$	$1.491^{+0.052}_{-0.100}$	$1.93^{+1.25}_{-0.49}$	$1.211^{+0.088}_{-0.033}$	$4.48^{+1.70}_{-1.15}$

We repeat this calculation for the 2σ contour (which extends into the northeast region of the dotted white Complex A contour in Figure 3) and different $P_{\rm thresh}$ levels. We report the resulting galaxy overdensity and structure total mass in Table 5. The scatter in overdensity and mass measurements is primarily driven by wider Gaussian kernel bandwidths optimized to fewer data points (larger bandwidths produce larger measured volumes, which enclose different galaxies to change the overdensity measurement).

6.2. Galactic Conformity

Of the six $z \gtrsim 3$ spectroscopically confirmed COSMOS protoclusters we have examined in this work (solid stars), two stand out in that they exhibit elevated quenched fractions and have quiescent UMGs (MAG-0959 and QO-1000). The other four protoclusters (VPC-1000, RO-1001, MAG-1001, and MAG-1000) all host star-forming UMGs and have low quiescent fractions, which are consistent with the field (Table 4). It appears that these protoclusters obey galactic conformity: protoclusters with quiescent "centrals" have higher fractions of quiescent members, while protoclusters with star-forming "centrals" have higher fractions of star-forming members (i.e., lower quiescent fractions) and are more consistent with the field population (e.g., J. I. Phillips et al. 2014).

Though studies of the galaxy stellar mass function indicate that, as a whole, the quiescent fraction of the protocluster galaxy population does not differ significantly from the field (A. H. Edward et al. 2024; B. Forrest et al. 2024), the recent spectroscopic confirmation of quenched galaxies in overdensities have raised the question of the role environments play in massive galaxy evolution (e.g., M. Kubo et al. 2021; K. Ito et al. 2023; A. de Graaff et al. 2024; S. Jin et al. 2024; T. Kiyota et al. 2024; M. Tanaka et al. 2024; S. M. Urbano Stawinski et al. 2024). Quiescent fractions have been measured in the literature for just two other protoclusters with spectroscopically confirmed UMGs: the protocluster in SSA22 at $z = 3.09$ (hereafter, just "SSA22"; M. Kubo et al. 2013), and

the protocluster in SXDS at $z = 3.99$ (hereafter, just "SXDS"; M. Tanaka et al. 2024). We briefly summarize these last two structures here:

1. SSA22 at $z = 3.09$ is one of the most comprehensively studied high-redshift cosmic structures (e.g., C. C. Steidel et al. 1998; Y. Matsuda et al. 2005; B. D. Lehmer et al. 2009; Y. Tamura et al. 2009; M. W. Topping et al. 2016). A study of massive galaxies in SSA22 found ∼20% of $\log(M_\star/M_\odot) > 11$ galaxies had observed colors consistent with those of quiescent galaxies, and after correcting for background contamination the fraction increased to 50% (M. Kubo et al. 2013). The spectroscopic confirmation of a quiescent UMG (the most massive galaxy in SSA22) was presented in M. Kubo et al. (2021) and its massive quiescent partner in M. Kubo et al. (2022).
2. SXDS at $z = 3.99$ was also first identified and presented as an overdensity of quiescent galaxies in M. Tanaka et al. (2024). Spectroscopic follow-up confirmed the most massive quiescent galaxy with $\log(M_\star/M_\odot) > 11$ and combined spectrophotometric fitting supports the membership of another four $\log(M_\star/M_\odot) > 10$ quiescent galaxies. The authors also report that they measured a quiescent fraction of $36\% \pm 14\%$ in the protocluster and a few percent in the field.

We show the quiescent fractions of the protoclusters in Table 4 plus SSA22 and SXDS in Figure 6, where the points are color-coded blue or red based on whether the central UMG is star-forming or quiescent. The protoclusters from the literature also appear to obey the trend of galactic conformity, though we note that quiescent galaxies in these structures were selected by different methods than the one we used in our analysis (sources were classified as quiescent in SSA22 based on their observed $i - K$ and $K - [4.5\,\mu\mathrm{m}]$ colors and K-band magnitude, and in SXDS based on best-fit sSFR; M. Kubo et al. 2013; M. Tanaka et al. 2024).

In low-redshift studies, conformity is often demonstrated as a difference in the quenched fraction of satellites around quiescent and star-forming centrals (e.g., M. Ayromlou et al. 2021). This trend is then shown to persist, even as a function of, e.g., stellar mass or luminosity (of the central or satellites; W.-H. Wang et al. 2012), halo mass (S. M. Weinmann et al. 2006), local density (M. Treyer et al. 2018), redshift (L. Kawinwanichakij et al. 2016), or separation between the central and satellite (G. Kauffmann et al. 2013). Large data sets (e.g., the Sloan Digital Sky Survey; D. G. York et al. 2000) were necessary to robustly demonstrate conformity and its dependence (or lack thereof) on these factors. As quiescent fractions have been measured for only eight protoclusters with identifiable UMGs at $z \gtrsim 3$, we instead use the quiescent fraction and central UMG's star-forming/quiescent status in each protocluster as a proxy to show evidence for galactic conformity at $z \gtrsim 3$ for the first time.

6.2.1. Possible Mechanisms Driving Conformity?

While the existence of galactic conformity is generally well-established at low redshift, there is significant disagreement over cause of this trend. Are new physics or "hidden variables" required to explain galactic conformity, is conformity explained by known (e.g., environmental) processes, or is it simply a byproduct of halo bias and how galaxies cluster? The mechanism is unclear. It has been suggested that various

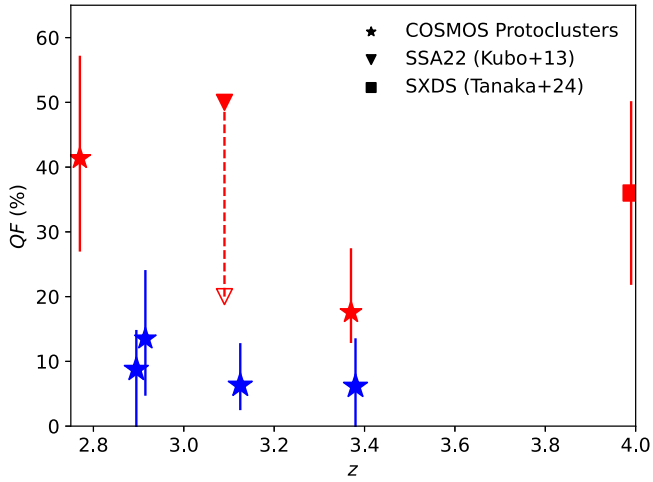

Figure 6. The measured quiescent fractions for the six COSMOS protoclusters explored in this work. The points and errorbars of each COSMOS protocluster are colored based on the rest-frame $U - V$ and $V - J$ colors of the protocluster's most massive spectroscopically confirmed UMG; if the UMG falls in the quiescent (star-forming) region (see Figure 5), the protocluster is colored red (blue). We also include quiescent fractions reported in the literature for SSA22 (the solid and open downward-facing triangles respectively show the corrected and uncorrected values; M. Kubo et al. 2013) and SXDS (the red square; M. Tanaka et al. 2024), both of which host quiescent UMGs. There is an observed trend that when the central UMG is *UVJ* star-forming, the protocluster has a quiescent fraction similar to the field (i.e., they are more star-forming) and when the central UMG is *UVJ* quiescent, the protocluster has an elevated quiescent fraction.

causes, such as AGN feedback affecting neighboring galaxies (G. Kauffmann 2015, 2018; M. Ayromlou et al. 2022; though see also B. M. B. Henriques et al. 2015; L. P. T. Sin et al. 2017, 2019), assembly bias (A. P. Hearin et al. 2015, 2016), or the star formation–density relationship (S. Sun et al. 2018), could produce the conformity signal at low redshift. Whether these mechanisms could also produce the observed trend at $z \gtrsim 3$ is also uncertain.

There is some evidence for radio AGN driving environmental quenching in $z \sim 1$ clusters (L. Shen et al. 2019), and a proto-ICM has been detected in the Spiderweb protocluster at $z = 2.156$ (the highest redshift detection of hot intracluster gas to date; L. Di Mascolo et al. 2023). While the UMG in MAG-0959 hosts an X-ray AGN (with luminosity $L_{2-10\,\mathrm{keV}} = (6.4 \pm 1.7) \times 10^{45}$ erg s^{-1}; Z. C. Marsan et al. 2017) and high fraction of X-ray AGNs are found in SSA22 (B. D. Lehmer et al. 2009; M. Kubo et al. 2022; E. B. Monson et al. 2023), it is unknown if such AGNs could be capable of heating a proto-intracluster medium especially on such short cosmic timescales at $z > 3$. Alternatively, the elevated quiescent fractions we see could simply be a result of AGN feedback affecting only their host galaxies in protoclusters with high AGN fractions.

A. P. Hearin et al. (2016) argued that halos undergoing interactions with neighboring halos give rise to correlated accretion histories (and therefore similar galaxy star formation histories) in large-scale environments, which produce the conformity signal at low redshift. The halos of high-redshift protocluster galaxies formed only recently (within the past ∼2 Gyr); therefore, galaxies found in protoclusters were almost necessarily born in overdense regions (not enough time has passed for significant populations of field galaxies to fall into the protocluster). However, despite the short dynamical timescales of the high-redshift Universe, insufficient time may have passed for accretion histories of halos (and the

evolution of the galaxies within those halos) in different large-scale environments to have significantly diverged. We also note that assembly bias has previously been invoked as a potential explanation for differing clustering populations (K. Shi et al. 2019, 2020) and elevated quenched fractions (K. Shi et al. 2021) in protoclusters. In such a scenario, the protoclusters with elevated quiescent fractions would be older or more mature and "relaxed" than protoclusters full of star-forming galaxies.

It has also been suggested that galactic conformity simply arises due to the dependence of a galaxy's star formation on the local density. S. Sun et al. (2018) argued that (at low redshift), no new physics were needed to explain conformity, and instead that star formation activity of neighboring galaxies is more strongly dependent on the local environment than it is on the star formation activity of a nearby massive central. Our work examines galaxies in protoclusters, which are more overdense than the field, but less dense than their low-redshift descendants. While it is possible that an early relationship between density and SFR plays a role in the apparent observed conformity, whether that relationship is correlation (B. C. Lemaux et al. 2022) or anticorrelation (N. Chartab et al. 2020) is also the subject of debate. Regardless of the relationship, we do not find a noticeable correlation between galaxy overdensity and quiescent fraction for the six COSMOS protoclusters presented here.

Although we cannot draw definitive conclusions about the cause of conformity, the observation of this apparent trend in $z \gtrsim 3$ protoclusters indicates that whatever process causes galactic conformity may be present at very early times. As many massive, quiescent centrals in the low-redshift Universe feature ancient stellar populations, if their satellites are similarly coeval, then conformity could be expected at the epoch of massive galaxy and protocluster quenching, $z \sim 2$–3. If galactic conformity is not unique to the $z < 2$ Universe, then the mechanism causing it must have been in place since at least the quenching of massive galaxies. Its presence at high redshift could rule out low-redshift quenching mechanisms (e.g., ram pressure stripping) as the primary drivers of conformity for galaxies in massive halos. A better understanding of how galaxies in protoclusters quench is key, as whichever mechanisms drive high-redshift quenching could be closely related to the mechanisms responsible for conformity in the low-redshift Universe.

7. Summary

We have carried out an analysis of six spectroscopically confirmed protoclusters containing UMGs in the COSMOS field. We measured quiescent fractions for each of the six protoclusters and proposed that they show evidence for galactic conformity at $z \gtrsim 3$. We also detailed protocluster MAGAZ3NE J100143 +023021 at $z = 3.12$, which is newly spectroscopically confirmed. Combining near-infrared MOSFIRE spectroscopy and the COSMOS2020 photometric catalogs, we calculated MAG-1001's redshift, cataloged its members and their properties, and estimated its mass. Our conclusions are as follows:

1. We found that MAG-1001 contains 28 spectroscopic and 51 photometric members within 10 comoving Mpc of (and including) the most massive confirmed spectroscopic galaxy. Three spectroscopic members were confirmed to have stellar masses in excess of $10^{11}\,M_{\odot}$. We utilized the biweight estimator to calculate a central protocluster redshift, $z = 3.122^{+0.004}_{-0.007}$.
2. We calculated galaxy overdensity and protocluster total mass of the MAG-1001 system, and quiescent fractions for all six COSMOS systems using different photometric selection $P_{\rm thresh}$ values. Quiescent fractions for the COSMOS protoclusters and the coeval field were found to be robust to these criteria, though at higher $P_{\rm thresh}$ (i.e., a stricter membership selection and therefore lower counts) uncertainties were larger. The overdensity and protocluster mass measurements for MAG-1001 exhibited more variation, though this was mainly due to the Gaussian kernel bandwidth optimization. We used $P_{\rm thresh} = 0.17$ as our fiducial selection criterion because lower P values produced similar quiescent fractions and did not over-smooth high-density structures in the density map.
3. We mapped protocluster MAG-1001 and its extended structure in the COSMOS field by applying a Gaussian kernel density estimator to massive galaxies from the C2020 photometric catalog, supplemented by spectroscopic redshifts. We found that our density map of massive galaxies at $z = 3.125$ closely matched the $z \sim 3.1$ LAE overdensity Complex A from V. Ramakrishnan et al. (2023), and we speculated that the MAG-1000/Complex A system could be a $z = 3.1$ protosupercluster like Hyperion (O. Cucciati et al. 2018) or Elentári (B. Forrest et al. 2023, 2024). The dense core of the protocluster spans 240 square cMpc, and we estimated its mass is $2.25^{+1.55}_{-0.65} \times 10^{14}\,M_{\odot}$ and galaxy overdensity $\delta_{\rm gal} = 1.450^{+0.165}_{-0.029}$. The extended region around the protocluster (which better matches the LAE overdensity) is estimated to have mass $4.78^{+1.30}_{-1.53} \times 10^{14}\,M_{\odot}$ and galaxy overdensity $\delta_{\rm gal} = 1.250^{+0.193}_{-0.005}$.
4. We identified member galaxies and central UMGs in the six $z \gtrsim 3$ COSMOS protoclusters. The galaxies were divided up into quiescent and star-forming populations based on their rest-frame colors, which allowed us to calculate quiescent fractions for each protocluster and coeval field sample. In protoclusters where the central UMG's rest-frame colors are consisted with ongoing star formation, we found that the quenched fraction was low and indistinguishable from the coeval field. Conversely, in protoclusters where the central UMG had quiescent rest-frame colors, the protocluster exhibited a high quenched fraction, elevated relative to the coeval field. We argued that this is tentative evidence for galactic conformity and is (to date) the highest redshift instance of its detection.
5. We speculated about the potential mechanism driving the observed apparent conformity. We discussed proposed causes for conformity at low redshift including AGN feedback, assembly bias, and the relationship between star formation and local density. While it is not clear if they could also produce conformity at $z \gtrsim 3$, the observed trend suggests that whatever mechanism causes galactic conformity at low redshifts could already be in place only 2 Gyr after the Big Bang.

Acknowledgments

We thank the anonymous referee for their helpful feedback and suggestions, which significantly improved our original

manuscript. I.M. thanks John Weaver, Katriona Gould, and Gabriel Brammer for discussions about COSMOS2020 and `EazyPy`. G.W. gratefully acknowledges support from the National Science Foundation (NSF) through grant AST-2205189 and from HST program number GO-16300. Support for program number GO-16300 was provided by NASA through grants from the Space Telescope Science Institute, which is operated by the Association of Universities for Research in Astronomy, Incorporated, under NASA contract NAS5-26555. M.C.C. and S.M.U.S. acknowledge support from the NSF through grant AST-1815475. D.M. acknowledges support by the NSF grant AST-2009442 and by the National Aeronautics and Space Administration (NASA) under award number 80NSSC21K0630, issued through the NNH20ZDA001N Astrophysics Data Analysis Program (ADAP). Some of the material presented in this paper is based upon work supported by the NSF under grant No. 1908422.

The data presented herein were obtained at the W. M. Keck Observatory, which is operated as a scientific partnership among the California Institute of Technology, the University of California and the National Aeronautics and Space Administration. The Observatory was made possible by the generous financial support of the W. M. Keck Foundation. The authors wish to recognize and acknowledge the very significant cultural role and reverence that the summit of Maunakea has always had within the indigenous Hawaiian community. We are most fortunate to have the opportunity to conduct observations from this mountain.

ORCID iDs

Ian McConachie https://orcid.org/0000-0002-2446-8770
Gillian Wilson https://orcid.org/0000-0002-6572-7089
Ben Forrest https://orcid.org/0000-0001-6003-0541
Z. Cemile Marsan https://orcid.org/0000-0002-7248-1566
Adam Muzzin https://orcid.org/0000-0002-9330-9108
M. C. Cooper https://orcid.org/0000-0003-1371-6019
Marianna Annunziatella https://orcid.org/0000-0002-8053-8040
Danilo Marchesini https://orcid.org/0000-0001-9002-3502
Percy Gomez https://orcid.org/0000-0003-0408-9850
Wenjun Chang https://orcid.org/0000-0003-2144-2943
Stephanie M. Urbano Stawinski https://orcid.org/0000-0001-8169-7249
Brian C. Lemaux https://orcid.org/0000-0002-1428-7036
Ekta A. Shah https://orcid.org/0000-0001-7811-9042
Priti Staab https://orcid.org/0000-0002-8877-4320
Lori M. Lubin https://orcid.org/0000-0003-2119-8151
Roy R. Gal https://orcid.org/0000-0001-8255-6560

References

Adelberger, K. L., Steidel, C. C., Giavalisco, M., et al. 1998, ApJ, 505, 18
Aihara, H., Armstrong, R., Bickerton, S., et al. 2018, PASJ, 70, S8
Ata, M., Lee, K.-G., Vecchia, C. D., et al. 2022, NatAs, 6, 857
Ayromlou, M., Kauffmann, G., Anand, A., & White, S. D. M. 2022, MNRAS, 519, 1913
Ayromlou, M., Kauffmann, G., Yates, R. M., Nelson, D., & White, S. D. M. 2021, MNRAS, 505, 492
Baldry, I. K., Glazebrook, K., Brinkmann, J., et al. 2004, ApJ, 600, 681
Balogh, M. L., Gilbank, D. G., Muzzin, A., et al. 2017, MNRAS, 470, 4168
Balogh, M. L., McGee, S. L., Mok, A., et al. 2016, MNRAS, 456, 4364
Barreira, A., Lazeyras, T., & Schmidt, F. 2021, JCAP, 2021, 029
Baxter, D. C., Cooper, M. C., Balogh, M. L., et al. 2022, MNRAS, 515, 5479
Baxter, D. C., Cooper, M. C., Balogh, M. L., et al. 2023, MNRAS, 526, 3716
Beers, T. C., Flynn, K., & Gebhardt, K. 1990, AJ, 100, 32
Berti, A. M., Coil, A. L., Behroozi, P. S., et al. 2017, ApJ, 834, 87
Bertin, E., & Arnouts, S. 1996, A&AS, 117, 393
Brammer, G. B., van Dokkum, P. G., & Coppi, P. 2008, ApJ, 686, 1503
Bray, A. D., Pillepich, A., Sales, L. V., et al. 2016, MNRAS, 455, 185
Brinch, M., Greve, T. R., Weaver, J. R., et al. 2023, ApJ, 943, 153
Calderon, V. F., Berlind, A. A., & Sinha, M. 2018, MNRAS, 480, 2031
Capak, P., Abraham, R. G., Ellis, R. S., et al. 2007, ApJS, 172, 284
Capak, P. L., Riechers, D., Scoville, N. Z., et al. 2011, Natur, 470, 233
Casey, C. M. 2016, ApJ, 824, 36
Casey, C. M., Cooray, A., Capak, P., et al. 2015, ApJL, 808, L33
Champagne, J. B., Casey, C. M., Zavala, J. A., et al. 2021, ApJ, 913, 110
Chapman, S. C., Blain, A., Ibata, R., et al. 2009, ApJ, 691, 560
Chartab, N., Mobasher, B., Darvish, B., et al. 2020, ApJ, 890, 7
Chiang, Y.-K., Overzier, R., & Gebhardt, K. 2013, ApJ, 779, 127
Chiang, Y.-K., Overzier, R., & Gebhardt, K. 2014, ApJL, 782, L3
Chiang, Y.-K., Overzier, R. A., Gebhardt, K., & Henriques, B. 2017, ApJL, 844, L23
Chiang, Y.-K., Overzier, R. A., Gebhardt, K., et al. 2015, ApJ, 808, 37
Conroy, C., & Gunn, J. E. 2010, ApJ, 712, 833
Conroy, C., Gunn, J. E., & White, M. 2009, ApJ, 699, 486
Cooper, M. C., Coil, A. L., Gerke, B. F., et al. 2010, MNRAS, 409, 337
Cooper, M. C., Newman, J. A., Coil, A. L., et al. 2007, MNRAS, 376, 1445
Cooper, M. C., Newman, J. A., Weiner, B. J., et al. 2008, MNRAS, 383, 1058
Cucciati, O., Lemaux, B. C., Zamorani, G., et al. 2018, A&A, 619, A49
Cucciati, O., Zamorani, G., Lemaux, B. C., et al. 2014, A&A, 570, A16
Daddi, E., Jin, S., Strazzullo, V., et al. 2017, ApJL, 846, L31
Daddi, E., Rich, R., Valentino, F., et al. 2022, ApJL, 926, 7
Daddi, E., Valentino, F., Rich, R. M., et al. 2021, A&A, 649, A78
Dannerbauer, H., Kurk, J. D., De Breuck, C., et al. 2014, A&A, 570, A55
Darvish, B., Scoville, N. Z., Martin, C., et al. 2020, ApJ, 892, 8
de Graaff, A., Setton, D. J., Brammer, G., et al. 2024, arXiv:2404.05683
Di Mascolo, L., Saro, A., Mroczkowski, T., et al. 2023, Natur, 615, 809
Diener, C., Lilly, S. J., Knobel, C., et al. 2013, ApJ, 765, 109
Diener, C., Lilly, S. J., Ledoux, C., et al. 2015, ApJ, 802, 31
Dressler, A. 1980, ApJ, 236, 351
Edward, A. H., Balogh, M. L., Bahe, Y. M., et al. 2024, MNRAS, 527, 8598
Elbaz, D., Daddi, E., Le Borgne, D., et al. 2007, A&A, 468, 33
Finoguenov, A., Guzzo, L., Hasinger, G., et al. 2007, ApJS, 172, 182
Foltz, R., Wilson, G., Muzzin, A., et al. 2018, ApJ, 866, 136
Forrest, B., Annunziatella, M., Wilson, G., et al. 2020a, ApJL, 890, L1
Forrest, B., Lemaux, B. C., Shah, E., et al. 2023, MNRAS, 526, L56
Forrest, B., Lemaux, B. C., Shah, E. A., et al. 2024, ApJ, 971, 169
Forrest, B., Marsan, Z. C., Annunziatella, M., et al. 2020b, ApJ, 903, 47
Forrest, B., Tran, K.-V. H., Broussard, A., et al. 2017, ApJL, 838, L12
Forrest, B., Wilson, G., Muzzin, A., et al. 2022, ApJ, 938, 109
Geach, J. E., Sobral, D., Hickox, R. C., et al. 2012, MNRAS, 426, 679
Giavalisco, M., Steidel, C. C., Adelberger, K. L., et al. 1998, ApJ, 503, 543
Gómez, P. L., Nichol, R. C., Miller, C. J., et al. 2003, ApJ, 584, 210
Goto, T., Yamauchi, C., Fujita, Y., et al. 2003, MNRAS, 346, 601
Gunn, J. E., & Gott, J. R. I. 1972, ApJ, 176, 1
Hall, P. 1982, Biometrika, 69, 383
Hartley, W. G., Conselice, C. J., Mortlock, A., Foucaud, S., & Simpson, C. 2015, MNRAS, 451, 1613
Hasinger, G., Capak, P., Salvato, M., et al. 2018, ApJ, 858, 77
Hearin, A. P., Behroozi, P. S., & van den Bosch, F. C. 2016, MNRAS, 461, 2135
Hearin, A. P., Watson, D. F., & van den Bosch, F. C. 2015, MNRAS, 452, 1958
Henriques, B. M. B., White, S. D. M., Thomas, P. A., et al. 2015, MNRAS, 451, 2663
Henriques, B. M. B., White, S. D. M., Thomas, P. A., et al. 2017, MNRAS, 469, 2626
Hildebrandt, H., Pielorz, J., Erben, T., et al. 2009, A&A, 498, 725
Horne, K. 1986, PASP, 98, 609
Hung, C.-L., Casey, C. M., Chiang, Y.-K., et al. 2016, ApJ, 826, 130
Hung, D., Lemaux, B. C., Cucciati, O., et al. 2024, arXiv:2410.00237
Ilbert, O., Arnouts, S., McCracken, H. J., et al. 2006, A&A, 457, 841
Ito, K., Tanaka, M., Valentino, F., et al. 2023, ApJL, 945, L9
Jin, S., Sillassen, N. B., Magdis, G. E., et al. 2024, A&A, 683, L4
Kalita, B. S., Daddi, E., D'Eugenio, C., et al. 2021, ApJL, 917, L17
Kauffmann, G. 2015, MNRAS, 454, 1840
Kauffmann, G. 2018, MNRAS, 475, L45
Kauffmann, G., Heckman, T. M., White, S. D. M., et al. 2003, MNRAS, 341, 33
Kauffmann, G., Li, C., & Heckman, T. M. 2010, MNRAS, 409, 491
Kauffmann, G., Li, C., Zhang, W., & Weinmann, S. 2013, MNRAS, 430, 1447

Kauffmann, G., White, S. D. M., Heckman, T. M., et al. 2004, MNRAS, 353, 713
Kawinwanichakij, L., Quadri, R. F., Papovich, C., et al. 2016, ApJ, 817, 9
Kerscher, M. 2018, A&A, 615, A109
Kiyota, T., Ando, M., Tanaka, M., et al. 2024, arXiv:2406.02849
Knobel, C., Lilly, S. J., Woo, J., & Kovač, K. 2015, ApJ, 800, 24
Koyama, Y., Polletta, M. d., Tanaka, I., et al. 2021, MNRAS: Letters, 503, L1
Kriek, M., Shapley, A. E., Reddy, N. A., et al. 2015, ApJS, 218, 15
Kubo, M., Uchimoto, Y. K., Yamada, T., et al. 2013, ApJ, 778, 170
Kubo, M., Umehata, H., Matsuda, Y., et al. 2021, ApJ, 919, 6
Kubo, M., Umehata, H., Matsuda, Y., et al. 2022, ApJ, 935, 89
Lacerna, I., Contreras, S., González, R. E., Padilla, N., & Gonzalez-Perez, V. 2018, MNRAS, 475, 1177
Larson, R. B., Tinsley, B. M., & Caldwell, C. N. 1980, ApJ, 237, 692
Lawrence, A., Warren, S. J., Almaini, O., et al. 2007, MNRAS, 379, 1599
Le Fèvre, O., Tasca, L. A. M., Cassata, P., et al. 2015, A&A, 576, A79
Lee, K.-G., Hennawi, J. F., White, M., Croft, R. A. C., & Ozbek, M. 2014, ApJ, 788, 49
Lee, K.-G., Hennawi, J. F., White, M., et al. 2016, ApJ, 817, 160
Lee, K.-S., Gawiser, E., Park, C., et al. 2024, ApJ, 962, 36
Lehmer, B. D., Alexander, D. M., Geach, J. E., et al. 2009, ApJ, 691, 687
Lemaux, B. C., Cucciati, O., Le Fèvre, O., et al. 2022, A&A, 662, A33
Lemaux, B. C., Le Fèvre, O., Cucciati, O., et al. 2018, A&A, 615, A77
Lemaux, B. C., Tomczak, A. R., Lubin, L. M., et al. 2017, MNRAS, 472, 419
Lemaux, B. C., Tomczak, A. R., Lubin, L. M., et al. 2019, MNRAS, 490, 1231
Lilly, S. J., Le Fèvre, O., Renzini, A., et al. 2007, ApJS, 172, 70
Man, Z.-Y., Peng, Y.-J., Shi, J.-J., et al. 2019, ApJ, 881, 74
Mao, Z., Kodama, T., Pérez-Martínez, J. M., et al. 2022, A&A, 666, A141
Marsan, Z. C., Marchesini, D., Brammer, G. B., et al. 2015, ApJ, 801, 133
Marsan, Z. C., Marchesini, D., Brammer, G. B., et al. 2017, ApJ, 842, 21
Marsan, Z. C., Muzzin, A., Marchesini, D., et al. 2022, ApJ, 924, 25
Matsuda, Y., Yamada, T., Hayashino, T., et al. 2005, ApJL, 634, L125
McConachie, I., Wilson, G., Forrest, B., et al. 2022, ApJ, 926, 37
McCracken, H. J., Milvang-Jensen, B., Dunlop, J., et al. 2012, A&A, 544, A156
McLean, I. S., Steidel, C. C., Epps, H., et al. 2010, Proc. SPIE, 7735, 77351E
McLean, I. S., Steidel, C. C., Epps, H. W., et al. 2012, Proc. SPIE, 8446, 84460J
Mei, S., Hatch, N. A., Amodeo, S., et al. 2023, A&A, 670, A58
Monson, E. B., Doore, K., Eufrasio, R. T., et al. 2023, ApJ, 951, 15
Moore, B., Katz, N., Lake, G., Dressler, A., & Oemler, A. 1996, Natur, 379, 613
Moustakas, J., Coil, A. L., Aird, J., et al. 2013, ApJ, 767, 50
Muldrew, S. I., Hatch, N. A., & Cooke, E. A. 2015, MNRAS, 452, 2528
Muldrew, S. I., Hatch, N. A., & Cooke, E. A. 2018, MNRAS, 473, 2335
Muzzin, A., Wilson, G., Demarco, R., et al. 2013, ApJ, 767, 39
Muzzin, A., Wilson, G., Yee, H. K. C., et al. 2012, ApJ, 746, 188
Nantais, J. B., van der Burg, R. F. J., Lidman, C., et al. 2016, A&A, 592, A161
Nelson, D., Springel, V., Pillepich, A., et al. 2019, ComAC, 6, 2
Newman, A. B., Rudie, G. C., Blanc, G. A., et al. 2020, ApJ, 891, 147
Oemler, A. J. 1974, ApJ, 194, 1
Oke, J. B., & Gunn, J. E. 1983, ApJ, 266, 713
Otter, J. A., Masters, K. L., Simmons, B., & Lintott, C. J. 2020, MNRAS, 492, 2722
Paranjape, A., Kovač, K., Hartley, W. G., & Pahwa, I. 2015, MNRAS, 454, 3030
Pavesi, R., Riechers, D. A., Sharon, C. E., et al. 2018, ApJ, 861, 43
Peng, Y.-j., Lilly, S. J., Kovač, K., et al. 2010, ApJ, 721, 193
Phillips, J. I., Wheeler, C., Boylan-Kolchin, M., et al. 2014, MNRAS, 437, 1930
Phillips, J. I., Wheeler, C., Cooper, M. C., et al. 2015, MNRAS, 447, 698
Ramakrishnan, V., Lee, K.-S., Artale, M. C., et al. 2024, arXiv:2406.08645
Ramakrishnan, V., Moon, B., Im, S. H., et al. 2023, ApJ, 951, 119
Ross, A. J., & Brunner, R. J. 2009, MNRAS, 399, 878
Saracco, P., Marchesini, D., La Barbera, F., et al. 2020, ApJ, 905, 40
Shen, L., Lemaux, B. C., Lubin, L. M., et al. 2021, ApJ, 912, 60
Shen, L., Tomczak, A. R., Lemaux, B. C., et al. 2019, MNRAS, 484, 2433
Shi, K., Lee, K.-S., Dey, A., et al. 2019, ApJ, 871, 83
Shi, K., Toshikawa, J., Cai, Z., Lee, K.-S., & Fang, T. 2020, ApJ, 899, 79
Shi, K., Toshikawa, J., Lee, K.-S., et al. 2021, ApJ, 911, 46
Sillassen, N. B., Jin, S., Magdis, G. E., et al. 2022, A&A, 665, L7
Sin, L. P. T., Lilly, S. J., & Henriques, B. M. B. 2017, MNRAS, 471, 1192
Sin, L. P. T., Lilly, S. J., & Henriques, B. M. B. 2019, MNRAS, 488, 234
Spitler, L. R., Labbé, I., Glazebrook, K., et al. 2012, ApJL, 748, L21
Steidel, C. C., Adelberger, K. L., Dickinson, M., et al. 1998, ApJ, 492, 428
Straatman, C. M. S., Labbé, I., Spitler, L. R., et al. 2015, ApJL, 808, L29
Straatman, C. M. S., Spitler, L. R., Quadri, R. F., et al. 2016, ApJ, 830, 51
Strateva, I., Ivezić, Ž., Knapp, G. R., et al. 2001, AJ, 122, 1861
Sun, S., Guo, Q., Wang, L., et al. 2018, MNRAS, 477, 3136
Tamura, Y., Kohno, K., Nakanishi, K., et al. 2009, Natur, 459, 61
Tanaka, M., Onodera, M., Shimakawa, R., et al. 2024, ApJ, 970, 59
Tomczak, A. R., Lemaux, B. C., Lubin, L. M., et al. 2017, MNRAS, 472, 3512
Tomczak, A. R., Lemaux, B. C., Lubin, L. M., et al. 2019, MNRAS, 484, 4695
Topping, M. W., Shapley, A. E., & Steidel, C. C. 2016, ApJL, 824, L11
Tran, K.-V. H., Alcorn, L. Y., Kacprzak, G. G., et al. 2017, ApJ, 834, 101
Treyer, M., Kraljic, K., Arnouts, S., et al. 2018, MNRAS, 477, 2684
Urbano Stawinski, S. M., Cooper, M. C., Forrest, B., et al. 2024, OJAp, 7, 46
van der Burg, R. F. J., Rudnick, G., Balogh, M. L., et al. 2020, A&A, 638, A112
van der Wel, A., Noeske, K., Bezanson, R., et al. 2016, ApJS, 223, 29
Wang, K., Peng, Y., & Chen, Y. 2023, MNRAS, 523, 1268
Wang, T., Elbaz, D., Daddi, E., et al. 2016, ApJ, 828, 56
Wang, W., & White, S. D. M. 2012, MNRAS, 424, 2574
Wang, W.-H., Barger, A. J., & Cowie, L. L. 2012, ApJ, 744, 155
Weaver, J. R., Kauffmann, O. B., Ilbert, O., et al. 2022, ApJS, 258, 11
Weaver, J. R., Zalesky, L., Kokorev, V., et al. 2023, ApJS, 269, 20
Webb, K., Balogh, M. L., Leja, J., et al. 2020, MNRAS, 498, 5317
Weinmann, S. M., van den Bosch, F. C., Yang, X., & Mo, H. J. 2006, MNRAS, 366, 2
Whitaker, K. E., Labbé, I., van Dokkum, P. G., et al. 2011, ApJ, 735, 86
Williams, R. J., Quadri, R. F., Franx, M., van Dokkum, P., & Labbé, I. 2009, ApJ, 691, 1879
Wuyts, S., Labbé, I., Franx, M., et al. 2007, ApJ, 655, 51
York, D. G., Adelman, J., Anderson, J. E., Jr., et al. 2000, AJ, 120, 1579
Yuan, T., Nanayakkara, T., Kacprzak, G. G., et al. 2014, ApJL, 795, L20
Zavala, J. A., Casey, C. M., Scoville, N., et al. 2019, ApJ, 887, 183
Zu, Y., & Mandelbaum, R. 2018, MNRAS, 476, 1637